THESIS

SYNTHESIS OF MONOLAYER MoS_2 VIA CHEMICAL VAPOR DEPOSITION

Submitted by

Travis Varra

Department of Chemistry

In partial fulfillment of the requirements

For the Degree of Master of Science

Colorado State University

Fort Collins, Colorado

Spring 2020

Master's Committee:

Advisor: Justin Sambur

Amy Prieto
Mustafa Yourdkhani

Copyright by Travis Varra 2020

All Rights Reserved

ABSTRACT

SYNTHESIS OF MONOLAYER MoS_2 VIA CHEMICAL VAPOR DEPOSITION

Two-dimensional materials, specifically transition metal dichalcogenides (TMDs), have emerged as ideal candidates for lightweight and flexible optoelectronic applications. Unlike bulk solids, single layer TMDs exhibit a direct bandgap that makes next-generation device applications possible. This work describes the synthesis of single layer MoS_2 via chemical vapor deposition (CVD). This method involves thermal vaporization of MoO_3 and S precursors in a tube furnace. The influence of reaction conditions (e.g., temperature, pressure, reaction holding time, carrier gas flow rate, and precursor separation distance) on MoS_2 sample morphology was quantified using optical microscopy. Isolated equilateral triangles with $11\ \mu m$-long edge lengths were reproducibly grown on Si/SiO_2 substrates. The layer thickness was determined using Raman and photoluminescence spectroscopy.

ACKNOWLEDGEMENTS

I would like to thank the Sambur Group, specifically Dr. Justin Sambur, Michael Van Erdewyk, Dr. Li Wang, and Zach Nilsson. I would also like to thank Jacob Schneider for his conversations and contributions. I would like to give a special thanks to Dr. Amy Prieto for allowing me to use her lab's CVD set up to run the reactions.

TABLE OF CONTENTS

ABSTRACT ii

ACKNOWLEDGEMENTS iii

CHAPTER 1: PROPERTIES OF 2D MATERIALS, SPECIFICALLY TRANSITION METAL DICHALCOGENIDES, AND THEIR MONOLAYER GROWTH METHODS 1

1.1 2D Materials 1

1.2 Transition Metal Dichalcogenides (TMDs) 2

1.3 Preparation of monolayer TMDs 3

1.4 Chemical vapor deposition (CVD) 4

1.5 CVD growth of monolayer MoS_2 5

CHAPTER 2: MONOLAYER MoS_2 GROWTH VIA CHEMICAL VAPOR DEPOSITION 7

2.1 Experimental set up, methods, and image analysis procedure 7

2.1.1 Molecular powder precursors and growth substrates 7

2.1.2 Tube furnace set up 8

2.2 Initial reaction conditions en route to reaction optimization studies 9

2.3 Optical microscope and scanning electron microscopy imaging analysis procedure 11

2.4 Sample morphology of initial growth conditions 13

2.5 Optimizing precursor separation and substrate position 15

2.6 Optimizing reaction pressure 17

2.7 Maximum holding temperature 19

2.8 Optimizing carrier gas flow rate 20

2.9 Optimizing reaction hold time 22

CHAPTER 3: SPECTROSCOPIC CHARACTERIZATION OF CVD-GROWN MoS_2 24

3.1 CVD growth on large Si/SiO_2 substrates for spectroscopic characterization 24

3.2 Raman spectroscopy 27

3.3 Photoluminescence spectroscopy 29

3.4 Correlating PL intensity and Raman peak shifts for layer-thickness characterization 31

CHAPTER 4: CONCLUSIONS AND DIRECTIONS FOR FURTHER OPTIMIZATION 34

REFERENCES 37

CHAPTER 1: PROPERTIES OF 2D MATERIALS, SPECIFICALLY TRANSITION METAL DICHALCOGENIDES, AND THEIR MONOLAYER GROWTH METHODS

1.1 2D Materials

Two-dimensional (2D) materials are compounds where the lateral size far exceeds the material's thickness. More quantitatively, lateral sizes range from ~1-10,000 μm with single layer thickness being less than 1 nm [**1**]. Lateral size however, is only theoretically limited by the size of the growth substrate for bottom-up synthesis methods, or the size of the initial crystal for bulk exfoliation methods. 2D materials were first discovered and analyzed through the exfoliation of naturally occurring minerals such as graphite (graphene) and molybdenite (MoS_2) **[2]**. These materials form layered structures in their bulk crystals **[3]**. When reduced to a monolayer thickness, 2D materials exhibit different properties than their bulk crystal counterparts.

The most commonly known 2D material is graphene, which consists of single-atom thick carbon layers. Graphene is a transparent, flexible, thermally conductive material, with record charge carrier mobility of 200,000 $cm^2/V\ s$ **[4]**. These unique properties can be exploited for future applications in touch panel displays, computer and television displays, and light-emitting diodes (LEDs) **[5-6]**. Aside from graphene, three-atom thick transition metal dichalcogenides (TMDs) are a large group of 2D layered materials. These materials have bandgaps between ~1-2 eV, MoS_2 (1.23-1.89 eV), $MoSe_2$ (1.09-1.57 eV), and WSe_2 (1.20-1.66 eV), which align with the solar spectrum, making these materials candidates for solar energy conversion **[7]**.

1.2 Transition Metal Dichalcogenides (TMDs)

Transition metal dichalcogenides with the formula of MX_2, where M is usually a Group 6 transition metal (typically molybdenum or tungsten), covalently bonded to chalcogen atoms, X, (typically sulfur or selenium), in the form X-M-X. In bulk crystals, these form three-atom thick layers that are held together by van der Waals forces **[7]**.

The most common crystal structure of TMDs are the 2H phase, where each individual layer's atoms are slightly shifted from vertical alignment. Other common TMD crystal types are the 1T and 3R phases **[8]**. The number in the phase identifies the number of layers in the unit cell, and the letter denotes the symmetry around the transition metal, hexagonal, tetrahedral, and rhombohedral (Figure 1). Changes in crystal phase can have drastic effects on the properties and function of these materials. For example, the 2H phase of WS_2 is semiconducting, while the 1T phase is metallic, and MoS_2 is thermodynamically stable and semiconducting in the 2H phase, but has metastable and metallic behavior in the 1T phase **[9]**.

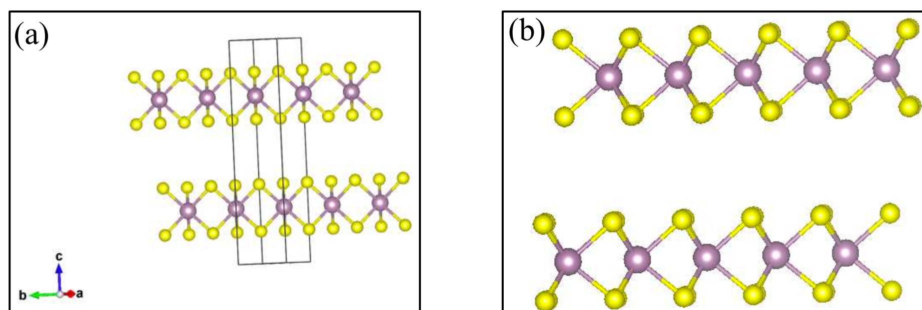

Figure 1: Diagram of (a) two-layer unit cell the MoS_2, and (b) cross-section of the shifted layer stacking of the 2H phase. Purple atoms represent the molybdenum and yellow represents sulfur.

These materials have fascinating photoelectrochemical properties which make the ideal for solar energy conversion, and the study of charge carrier separation and transport. Transition metal dichalcogenides have bandgaps between ~1.0 and 2.0 eV, which aligns with the visible solar spectrum, making these materials optimal for photovoltaic and photoelectrochemical study. A fascinating feature of these materials is that when their thickness is reduced to a monolayer, a

transformation from an indirect to a direct bandgap occurs. This can be seen in photoluminescence (PL) measurements. A direct bandgap allows for efficient charge carrier separation and recombination, and can be confirmed by the PL peak position and intensity **[10]**.

1.3 Preparation of monolayer TMDs

The first methods to obtain monolayer TMDs were top-down, either through mechanical or chemical exfoliation of bulk crystals. The weak van der Waal's forces, with binding energies of 40-70 meV, allow for ease of layer separation through exfoliation **[11]**. Molybdenum disulfide (MoS_2) has been studied since the 1960's, when it was first mechanically exfoliated down to 3-10 nm thicknesses from bulk naturally occurring molybdenite crystals **[12]**. The Scotch tape method that was developed to exfoliate graphene, was used more recently to mechanically exfoliate bulk TMD crystals down to single, or monolayer. This method has since evolved past Scotch tape to more refined adhesives or polymers, such as polymethyl methacrylate (PMMA) films and low residue adhesive tapes **[13]**. This process was able to achieve the monolayer samples used for the discovery and analysis of the unique properties of these materials, but with little control over size and layer thickness. Chemical exfoliation methods, like liquid-phase exfoliation (LPE), use ultrasonication and a solvent, commonly *N-methyl-pyrrolidone* (NMP), to separate the individual layers. Zhang et al. were able to produce 10-30 μm MoS_2 nanosheets through hydrazine intercalation, using sodium naphthalenide **[14]**. Chemical exfoliation methods can also result in a crystal phase transformation. Through the lithium intercalation of n-butyllithium in hexane into bulk MoS_2 crystals, and the reaction with water, generates a hydrogen evolution reaction (HER) as well as a 2H to 1T phase transformation. In MoS_2 this is caused by the slight shifting, or aligning, of layers **[15]**.

Electrochemical exfoliation in combination with LPE is also an effective way of obtaining monolayer TMDs from bulk crystals. Through the lithiation of $LiPF_6$ in ethyl/dimethyl carbonate, Zeong and colleagues were able to obtain a 92% yield of monolayer MoS_2 **[16]**. These top-down methods prove effective for obtaining large monolayer films, but the size and layer thickness was difficult to consistently control. Additionally, exfoliated naturally occurring crystals contain a large number of impurities, and lab grown bulk crystals still have to be exfoliated down to monolayer, and so, bottom-up synthesis methods were developed.

Chemical vapor transport (CVT) is a bottom-up synthesis method that artificially mimics the natural geological growth through the recrystallization of single bulk crystals. Precursor compounds are volatilized and react through heating, and are transported by a halogen gas in a two-zone, temperature gradient, tube furnace **[17]**. This bottom-up growth method was efficient in growing single bulk TMD crystals, but ineffective for mono or single-layer growth **[18]**. Another bottom-up method of synthesis involves the vaporization of solid precursors at high temperatures and pressures. Aqueous precursor solutions of ammonium molybdate ($(NH_4)_6Mo_7O_{24}$) and thiourea (CH_4N_2S) have been combined to hydrothermally synthesize MoS_2 **[19]**. Again, monolayer growth was difficult to control using this method.

1.4 Chemical vapor deposition (CVD)

Chemical vapor deposition (CVD) is a method of monolayer TMD synthesis from initial molecular precursors. In a quartz tube, the powder precursors are placed in separate physical locations at different temperature regions in a tube furnace (Figure 2). The precursors are heated to a high temperature (700-900 ºC), where the sublimation of the precursors occurs. Ideally, a two-temperature-zone furnace would be used in order to control the separate temperatures of the precursors because of the large difference in melting points. The transition metal precursors

typically have a much larger melting point than the chalcogen precursor (mp MoO_3 = 795 °C and mp sulfur = 120 °C). An inert (Ar or N_2), or slightly reducing (H_2), carrier gas is flowed through the quartz tube in order to bring the vaporized precursors together. Growth substrates are also placed inside the tube where the vaporized precursors react, nucleate, and grow [**20 & 21**].

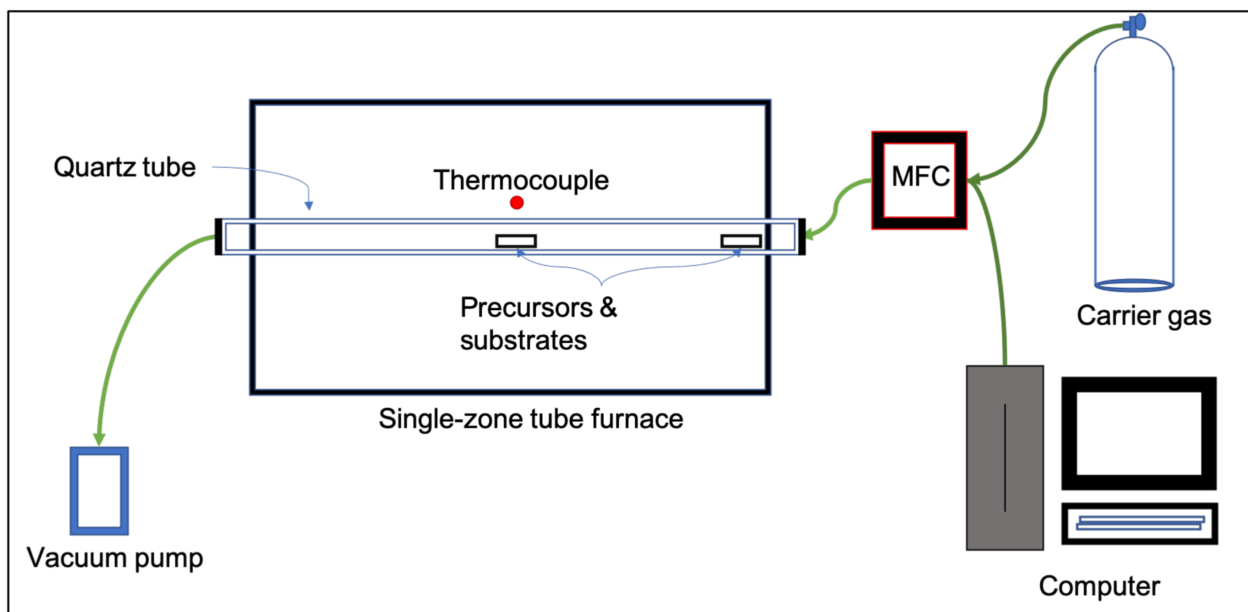

Figure 2: Diagram of a general CVD set up with single-zone tube furnace, quartz tube, reaction boats, molecular precursors, growth substrates, carrier gas, mass flow controllers (MFC), vacuum pump, and computer set up.

1.5 CVD growth of monolayer MoS_2

Bulk crystal and exfoliated molybdenum disulfide (MoS_2) have been a well-studied material since the 1960's, as discussed in Chapter 1.3. Mechanical and electrochemical exfoliation was successful in obtaining monolayer MoS_2, but control over particle size was inconsistent. After the discovery and CVD synthesis of graphene, additional 2D materials followed to investigate their unique properties **[22]**. The CVD synthesis of monolayer MoS_2 has been a focus of fundamental study over the past decade.

In CVD synthesis, the precursor vapor environment at the growth substrate is what influences particle size and controls morphology. The ratio of molybdenum to sulfur precursor

vapors dictates the kinetic growth dynamics at the MoS_2 particle edges **[23]**. Triangular morphologies are known to have sulfur terminated edges, where hexagonal morphologies have alternating molybdenum and sulfur terminated edges **[24]**. By manipulating variables such as precursor separation, temperature, reaction holding time, and carrier gas flow rate, controlled and reproducible growth of large area monolayer MoS_2 films and particles was achieved **[25]**.

The most common CVD growth substrates for monolayer MoS_2 are silicon wafers or sapphire **[26]**. The silicon wafers have an amorphous surface oxide layer, between ~150-300 nm (Si/SiO_2), in order to aid in the nucleation and particle growth **[27]**. Position and location of the substrates plays a role in the particle size and morphology. Vertically aligned substrates are more beneficial for MoS_2 films, whereas substrates placed oxide-layer-side down, yield triangular and hexagonal morphologies **[28]**. The molecular solid powder precursors can also vary in composition and amount used per reaction. Some common starting precursors include MoO_3 and sulfur for the synthesis of MoS_2, and flakes can be used in place of a fine grain powder **[29]**.

The chemical vapor deposition synthesis allows for growth of monolayer MoS_2 that is ideal for the fundamental investigation of electrochemical, optical, and electrical properties of TMD materials. This project focuses on growing monolayer MoS_2 using a custom CVD system.

.

CHAPTER 2: MONOLAYER MoS_2 GROWTH VIA CHEMICAL VAPOR DEPOSITION

2.1 Experimental set up, methods, and image analysis procedure

Due to the potential high quality, reproducibility, and size of particle growth of the of single layer TMDs [**30**], the bottom-up synthesis method of chemical vapor deposition was chosen. The Si/SiO_2 growth substrates were selected due to their low cost and common use among literature, as well as the MoO_3 and sulfur powder molecular precursors. Li et al. was able to reproducibly CVD grow monolayer MoS_2 in a high yield and with controlled size and morphology **[31]**. The following chapter will discuss the experimental set up, detailed growth procedures, and image analysis procedures for the CVD growth of monolayer MoS_2.

2.1.1 Molecular powder precursors and growth substrates

Following the general conditions developed by Li et al., **[31]** 10 mg of sulfur powder (Sigma-Aldrich 99.5% Lot #MKCG4576) and 2 mg of MoO_3 powder (Sigma-Aldrich, reagent grade Lot #MKCC4576) were weighed out and placed into separate alumina boats. Figure 4 shows the position of the boats inside the quartz tube. The boats were placed 16.5 cm apart, at separate regions of the quartz tube to achieve the different temperature regions for the individual precursors. The large difference in melting point temperatures (MoO_3 = 795 ºC and S = 120 ºC) required a spatial separation otherwise the sulfur powder will completely vaporize before the MoO_3.

A thermal oxide layer of ~150-300 nm was grown on a 100 mm silicon wafer (University Wafer ID:452). The wafer was placed in a box furnace (Lindberg/Blue M 1100 ºC) and heated to 1100 ºC for ~4 hr 5 min. The heating temperature and growth time were calculated using the University Wafer oxide layer calculator, and based on the oxygen environment (dry) and lattice orientation (<100>) **[32]**. The thermal oxide layer thickness can be approximated by the color of

the wafer after the oxide growth process **[33]**. The ~150-300 nm oxide layer thickness was estimated according to the color of the substrates after heating, which ranged from a gold to copper-colored to dark blue as the thickness increased (Figure 3). Once cooled, the wafer was cut into smaller (1.5 cm x 1.8 cm) pieces and cleaned using ultra-pure water and ethanol. The cut and cleaned Si/SiO_2 wafers were numbered and placed at measured distances downstream from the MoO_3 precursor, resting thermal oxide (reflective) side down on the alumina boat edges.

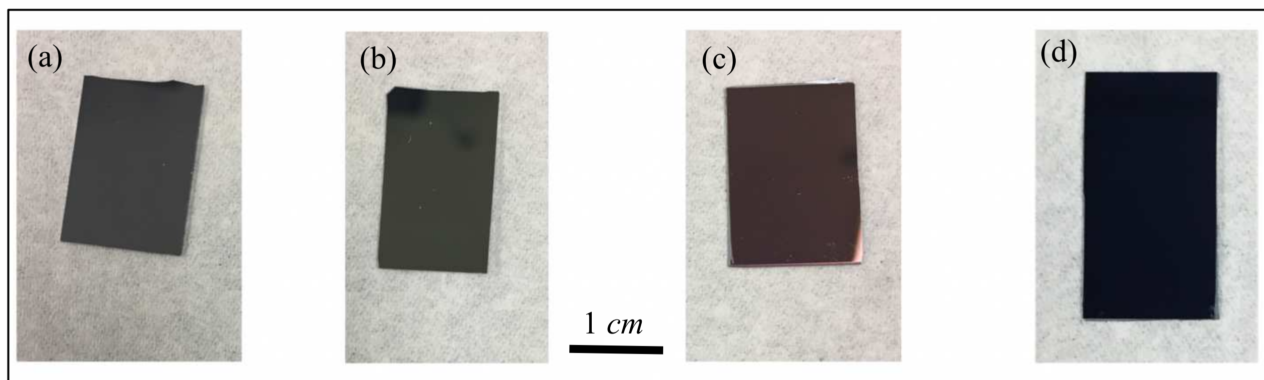

Figure 3: Photographs of Si/SiO_2 substrates. The different colors represent different thermal oxide layer thicknesses (a) initial substrate with ~2.5 nm oxide layer thickness, (b) ~175 nm thickness, (c) ~250 nm thickness, and (d) ~300 nm thickness.

2.1.2 Tube furnace set up

Figure 4 shows the experimental setup. A one-inch diameter, twenty-four-inch-long, quartz tube was placed in the tube furnace (Lindberg Blue M Model #TF55035COMA-1). The alumina boat containing the MoO_3 was placed at the center of the furnace, defined as 0.0 cm from the thermocouple. Additionally, the Si/SiO_2 substrates were placed thermal oxide side down on top of the boat at different distances from the MoO_3 precursor. The MoO_3 and Si/SiO_2 containing boat was aligned in the tube directly even with the furnace's thermocouple as shown in Figure 4. The sulfur-containing alumina boat was placed at the upstream edge of the furnace, 14.0-16.0 cm from the thermocouple (Figure 4). The reaction tube was connected to the vacuum pump (Ulvac G100-DC) and argon carrier gas line.

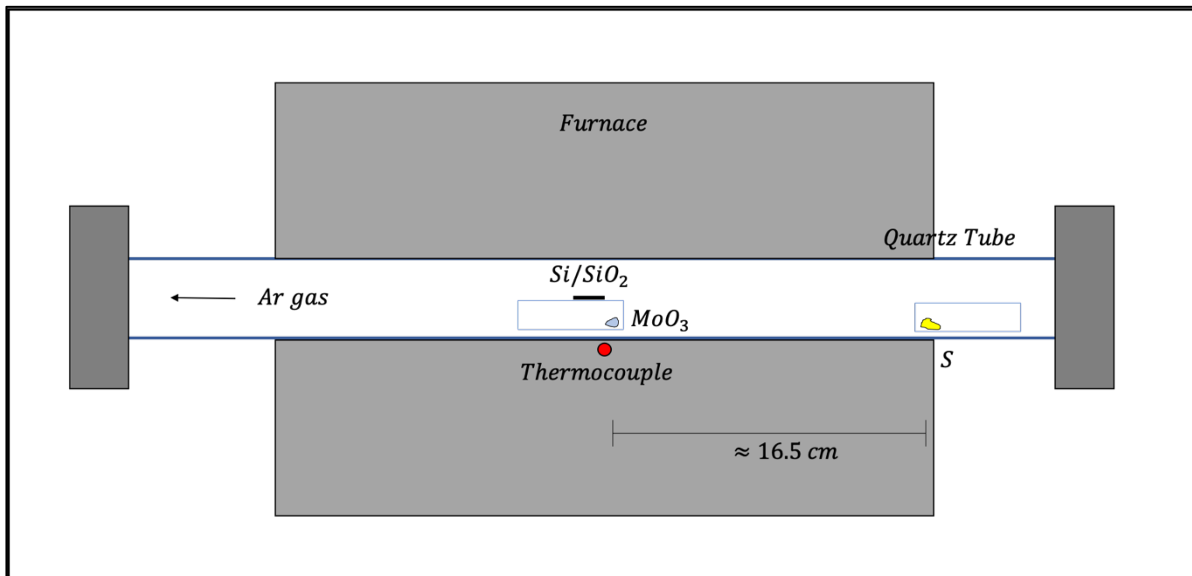

Figure 4: Diagram of the tube furnace set up. The MoO_3 precursor and Si/SiO_2 substrates placed at the thermocouple. The sulfur precursor was placed at the edge of the furnace (16.5 cm) upstream from thermocouple. Inert argon carrier gas flows from right to left.

2.2 Initial reaction conditions en route to reaction optimization studies

This section discusses an initial reaction condition that produced ~1-micron wide monolayer MoS_2 triangles. The MoO_3 and S precursors were placed 16.0 cm apart. The flow rate of the inert argon carrier gas was 100 sccm (standard cubic centimeters per minute), controlled by mass flow controllers (Sierra, Smart Trak 100), and run by LabView software. The sealed quartz tube was purged of oxygen/moisture for ~45 min before heating began. This pump-purge procedure began with pulling vacuum for 10-minutes, followed by alternating flowing 400 sccm and 0 sccm in 5-minute intervals, controlled through the LabView software. After two cycles of the 400 sccm pump-purge, the flow rate was changed to 300 sccm and the pressure was ramped up to a maintained pressure of 710 torr (0.934 atm). Once the pressure was reached the setpoint, the argon gas was reduced to 100 sccm and held for 5-minutes. A three-segment heating cycle was used for the growth run. The temperature was ramped to 800 °C over a thirty-minute period, held at the maximum temperature for a reaction hold time of 15 minutes, and then allowed to cool back

to room temperature (~45 minutes). These reaction conditions produced 1.5 μm MoS_2 equilateral morphologies as seen in Figure 5.

Figure 5: SEM image of triangular morphologies from the initial reaction conditions. The MoO_3 and S precursors were placed 16.0 cm apart. The pressure was held at 710 torr throughout the reaction. The maximum temperature used was 800 °C, for the 15 min hold time reaction.

When the sulfur was placed at the furnace edge (16.5 cm upstream from thermocouple), the sulfur powder did not fully vaporize, leaving behind a small, solidified darkened yellow chunk. When moved slightly inside of the furnace (16.0 cm upstream from thermocouple), almost all of the sulfur powder was vaporized during the reaction, resulting in ~0.5 cm from the upstream edge of the furnace being the optimal position for vaporization of the sulfur precursor. The heating of the sulfur surpassed the melting point, 120 ºC, but only reaching a max temperature of 225.0 ºC (Figure 6c). The temperature at the sulfur position was measured by attaching a thermometer and running the heating and flow cycle without the alumina boats, substrates, and precursors present.

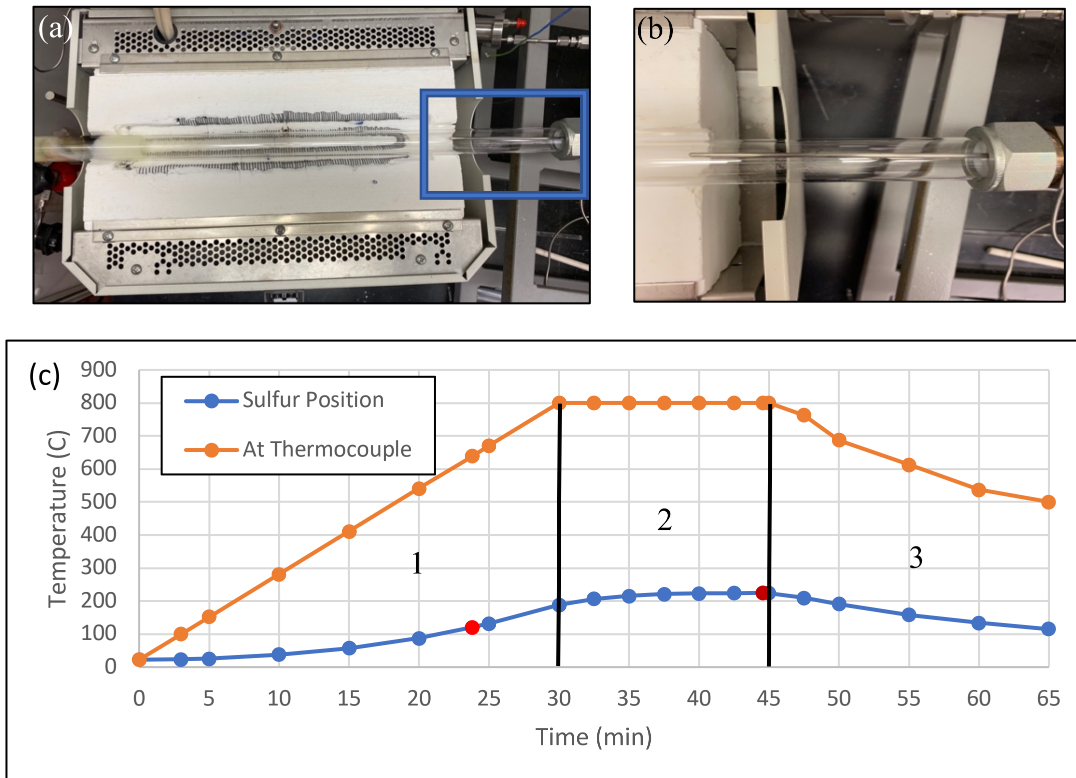

Figure 6: (a-b) Photographs of thermocouple placement for temperature measurements. (c) Temperature profiles of the three-step CVD growth process (orange line) and of temperature measured ~16.0 cm upstream from the thermocouple (blue line). Red markers represent the melting point of sulfur (~120 ºC) and the maximum temperature reached (225 ºC). The three-segment heating cycle is labeled 1, 2, and 3 representing the ramping to 800 ºC, holding time, and cooling respectively.

2.3 Optical microscope and scanning electron microscopy imaging analysis procedure

The sample morphology was characterized using an Olympus BX52 optical microscope that was equipped with an Olympus DP22 digital camera. 10x, 50x, and 100x microscope objectives (UMPlan) with 0.30, 0.80, and 0.90 numerical apertures, respectively, were used for image acquisition. The optical images were taken using the Olympus CellSens software (Figure 7b-d). For the qualitative optical analysis, triangle morphologies were considered monolayer thickness, consistent with literature **[34]**. Chapter 3 shows spectroscopic measurements that validate that assumption.

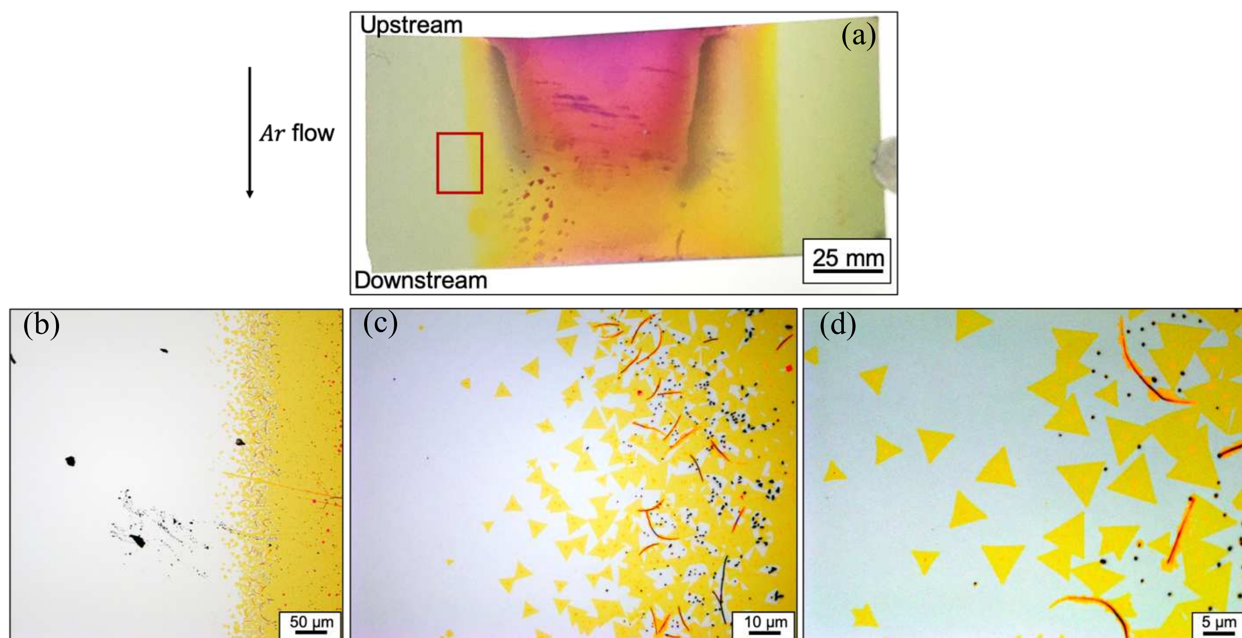

Figure 7: (a) Photograph of thermal oxide-layer side of growth substrate with highlighted zoomed triangle growth region. (b) Optical microscope image if triangular morphology at $10x$ magnification, (c) $50x$ magnification, and (d) $100x$ magnification.

ImageJ software was used to analyze the SEM and optical reflection images. Figure 8a shows a representative SEM image of a CVD-grown MoS_2 sample. Scanning electron microscopy (SEM) was performed using a JEOL 6500 FE-SEM and JEOL PC-SEM software. Figure 8b shows a cropped image of a single MoS_2 triangle. A line profile was drawn from corner to corner of the equilateral triangles to measure the particle edge length. The edge length distribution from 100 objects is shown in Figure 8c. The population was fit with a Gaussian curve fit to determine an average particle size as well as standard deviation (Figure 8c). Triangles with edge lengths ≤0.4 µm were not included in the particle analysis due to the diffraction-limited resolution of optical microscope experiments. We characterized triangular MoS_2 objects only and did not consider continuous film or bulk-like objects on the substrate.

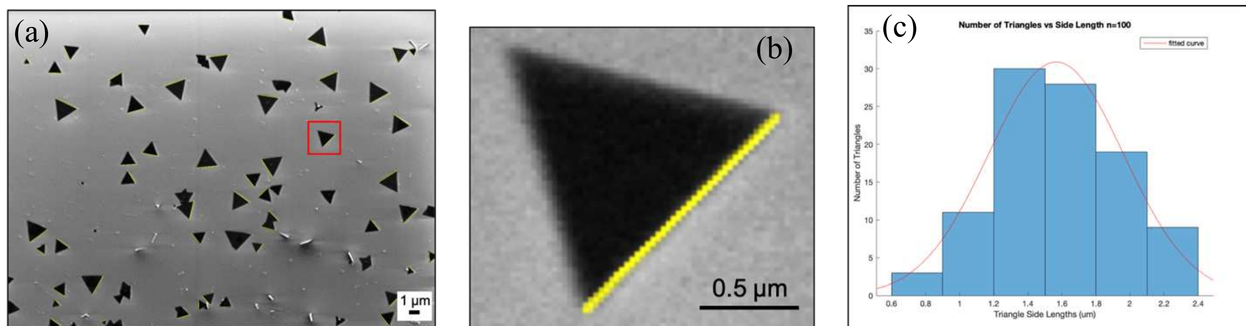

Figure 8: Image analysis of average monolayer triangular MoS_2 edge lengths. (a) SEM image of measured MoS_2 triangles. (b) Zoomed in SEM image of single measured triangle. (c) Particle growth size distribution and Gaussian fit curve with an average of ~1.55±0.42 µm, for a sample size of N=100.

2.4 Sample morphology of initial growth conditions

The initial growth conditions in Experimental Section 2.2 produced equilateral MoS_2 triangles. However, the triangles were only observed approximately ~200 µm from the substrate edge (as shown in Figure 9a-b). This was the region of the substrate that was hanging off of the alumina boat (Figure 9a).

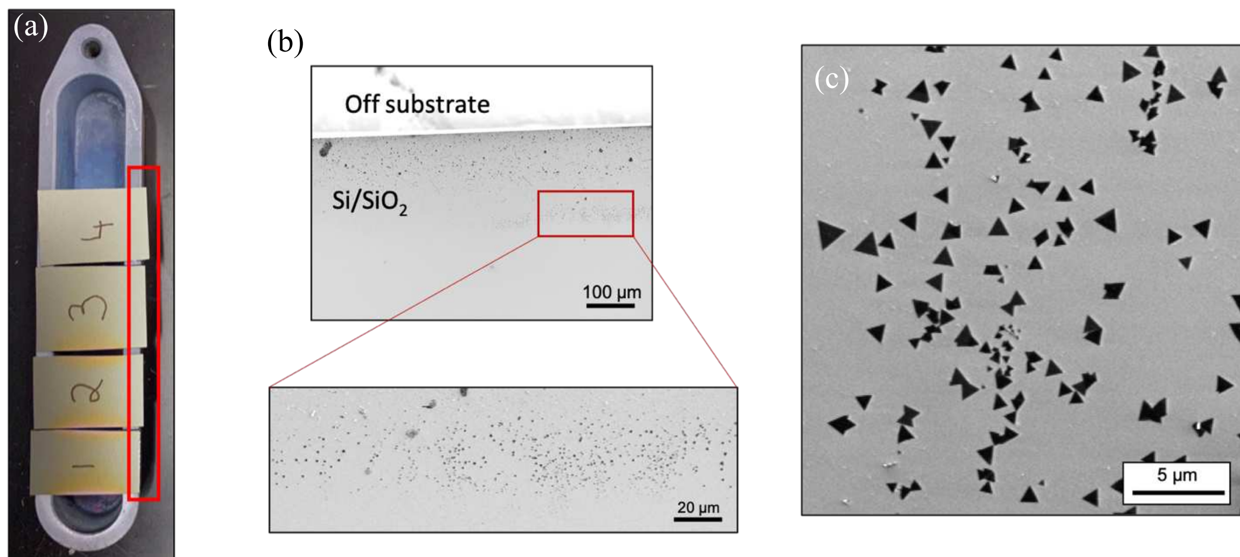

Figure 9: (a) Photograph of Si/SiO_2 substrates, oxide layer facing down, after the CVD reaction. The red rectangle indicates the sample region that produced MoS_2 triangles. (b) SEM image of substrate edge and zoomed in image MoS_2 growth region. (c) Further zoomed SEM image showing MoS_2 triangle morphology growth.

These CVD reactions produced MoS_2 material of various thicknesses on different regions on the substrates (Figure 10). Triangular monolayer MoS_2 growth occurred at the substrate edges and thick material grew in the center of the substrate (Figure 10b-d). Figure 10a shows a photograph of the substrate after MoS_2 growth. The photograph shows that the precursor flow likely causes the growth patterns. There is dense pink/purple contrast in the center of the substrate that indicates multi-layer growth. The light-yellow contrast indicates triangular monolayer and few-layer MoS_2 growth. By examining the entire substrate using the optical microscope, triangular morphologies were observed along the outside edges of the substrates as seen in Figure 10c.

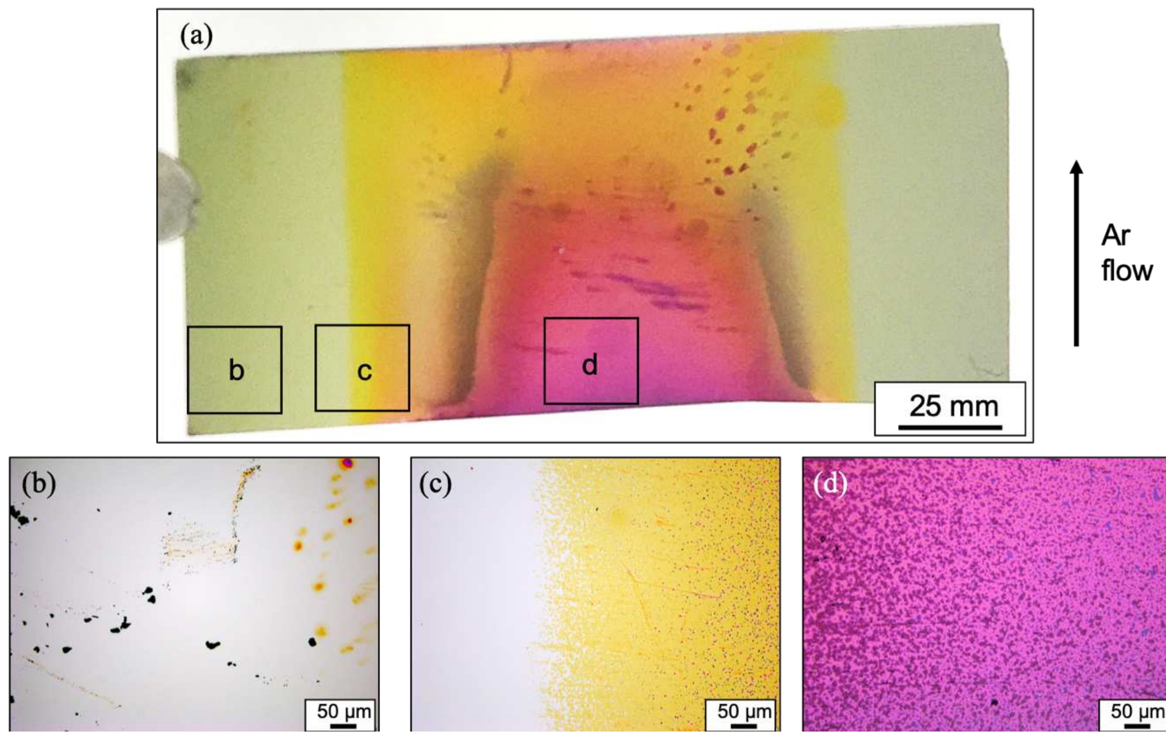

Figure 10: Three distinct regions on the Si/SiO_2 growth substrates. (a) Photograph of growth substrate with highlighted three-regions, (b) optical microscope image of outside of the boat edge region, (c) MoS_2 growth region, and a (d) densely covered center region. The regions were the same on both sides of the substrates. The 10x objective was used for these images.

2.5 Optimizing precursor separation and substrate position

We optimized the monolayer MoS_2 triangle size by varying reaction conditions in this single-zone tube furnace system. First, we studied the effect of precursor separation and substrate placement on the sample morphology. Özden et al. showed that the separation distance between the two precursors determines the edge length and morphology of monolayer MoS_2 **[28]**. We hypothesized that decreasing the separation distance would increase the MoS_2 growth rate because the smaller separation distance increases the concentration of precursor at the growth substrate. A separation distance of ~15.0 cm has been shown to yield monolayer MoS_2 particle growth **[35]**. By decreasing the distance, vaporized sulfur can travel down the tube leading to a larger precursor ratio. This creates a sulfur rich environment necessary for the reaction to occur **[23]**.

The two powder precursors were placed in the quartz tube at different locations relative to the furnace's thermocouple as discussed in the Tube Furnace Set Up section (2.1.2) and seen in Figure 11.

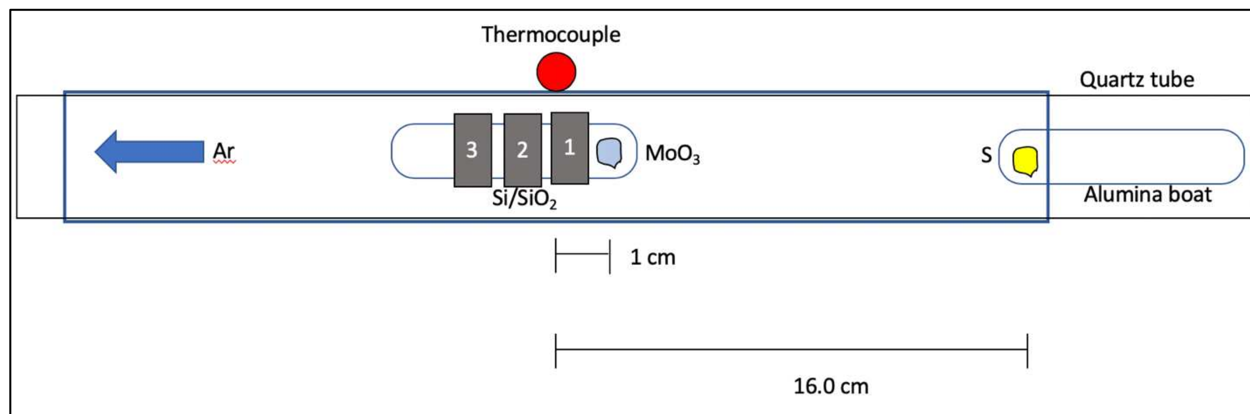

Figure 11: Diagram of the furnace, precursor, and substrate placement. Sulfur placed (16.0 cm) upstream from thermocouple, and MoO_3 1.0 cm upstream from thermocouple. Numbered Si/SiO_2 substrates placed thermal oxide layer side down on top of MoO_3 precursor boat. The substrates are place at different distances downstream from the MoO_3 precursor. Substrates 1, 2, and 3 represent downstream distances relative to the MoO_3 precursor centered around distances of ~1.25, ~2.8, and ~4.25 cm respectively.

A series of reactions were run with precursor separation distances of 16.0, 15.0, 14.5, and 14.0 cm. This was achieved by moving the MoO_3 precursor 0.0, 1.0, 1.5, and 2.0 cm upstream from the thermocouple (Figure 11). In the initial experiments, the starting distance between the sulfur and MoO_3 was ~16.0 cm, with the MoO_3 directly even with the furnace's thermocouple, and the sulfur 0.5 cm from the upstream edge, refer to Figure 4. The precursor ratios determine the kinetic growth dynamics and therefore determine the edge length and morphology **[28]**.

To study the influence of precursor separation, we varied the sulfur placement and performed CVD growth for a 15-minute holding time as discussed in Experimental Section 2.2 (Figure 5). The sulfur could not be moved further downstream because the increase in temperature would result in all of the powder vaporizing before the reaction could reach completion, resulting a small sulfur-to-molybdenum ratio. Additionally, the MoO_3 had a limit of how far upstream it could be moved without altering the maximum holding temperature.

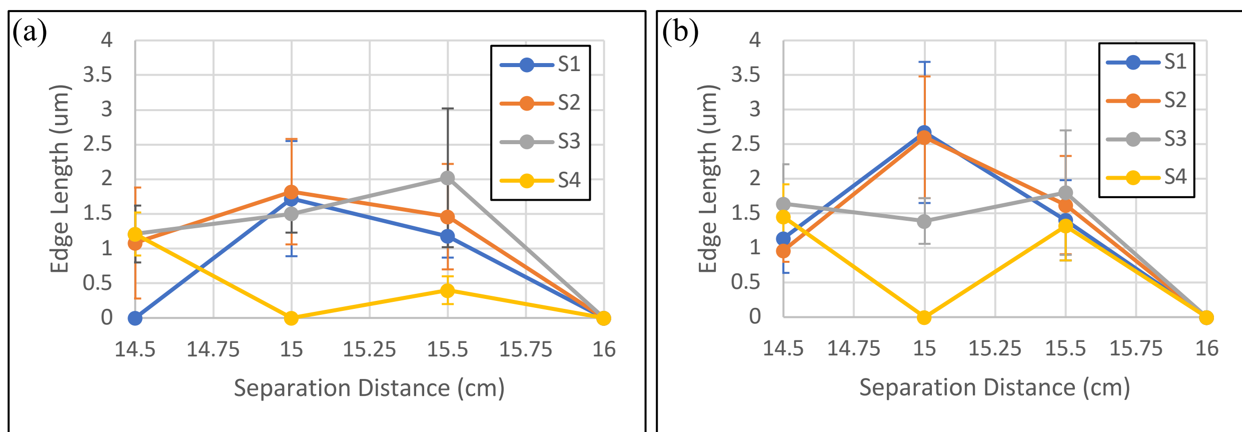

Figure 12: Plots of precursor separation distance versus edge length. Experimental separation distances of 16.0, 15.5, 15.0, 14.5 cm upstream from thermocouple. (a) Average particle size for left side of the substrates, and (b) right side of Si/SiO_2 substrate. Error bars are one standard deviation for N=100 measurements. Substrates S1, S2, S3, and S4 represent downstream distances relative to the MoO_3 precursor centered around distances of ~0.95, ~2.3, ~3.5, and ~4.6 cm respectively.

At a separation distance of 16.0 cm, triangular MoS_2 growth was only observed outside of the alumina boat (Figure 9). When the MoO_3 precursor is moved 0.5 cm upstream from the thermocouple, a separation distance of ~15.5 cm, triangular MoS_2 growth was observed on the inside of the boat region as seen in Figure 10c. The MoS_2 growth had moved from the outside of the boat region, to a more central region of the substrate (Figure 10b-c). When the separation is reduced to 15.0 cm, the largest particle edge length was observed on the substrates. Triangular particle growth uniformly covered the length of all four substrates, 0.5-5.25 cm downstream from MoO_3 precursor. Monolayer MoS_2 growth was located just outside of the densely covered center region as seen in Figures 10c. The largest average particle growth was located 0.5-3.5 cm downstream, with and average particle edge length of 1.75 ± 0.83 μm to 2.65 ± 1.02 μm (Figure 12). Yellow steaks were observed further downstream, 3.5-5.5 cm, containing very small (<0.4 μm) triangles. The largest isolated monolayer triangle edge length for the separation distance experiments was ~10.5 μm. These experiments were carried out at a maintained pressure of 600 torr. It was determined experimentally that a precursor separation distance of ~15.0 cm yielded the most reproducible, and largest average triangular monolayer MoS_2 growth (Figure 12). The average particle edge length size was sensitive to a ±0.5 cm change in separation distance (Figure 12). These results agree with the hypothesis that a precursor separation of distance of ~15.0 cm would yield reproducible and the largest monolayer edge lengths, having created a precursor ratio favorable to monolayer MoS_2 growth.

2.6 Optimizing reaction pressure

Having optimized the separation distance between precursors, we optimized the reaction pressure. We hypothesized that by reducing the maintained pressure from the in initial conditions (710 torr) to a local atmospheric pressure (~635 torr) would increase the monolayer MoS_2 particle

edge length. Lower pressures allow for a lower temperature substrate and a higher rate of deposition beneficial to monolayer MoS_2 growth **[36]**. Atmospheric pressure CVD (APCVD) is a known method of monolayer TMD growth, allowing for more uniform particles or films **[37]**. The effect of pressure on particle edge length and morphology was studied over the range of 575, 600, 635, 675, and 710 torr, as seen in Figure 13. This range was selected to examine the pressures at, and around atmospheric pressure (~635 torr). The pressure throughout the reaction was maintained through the LabView software and mass flow controllers.

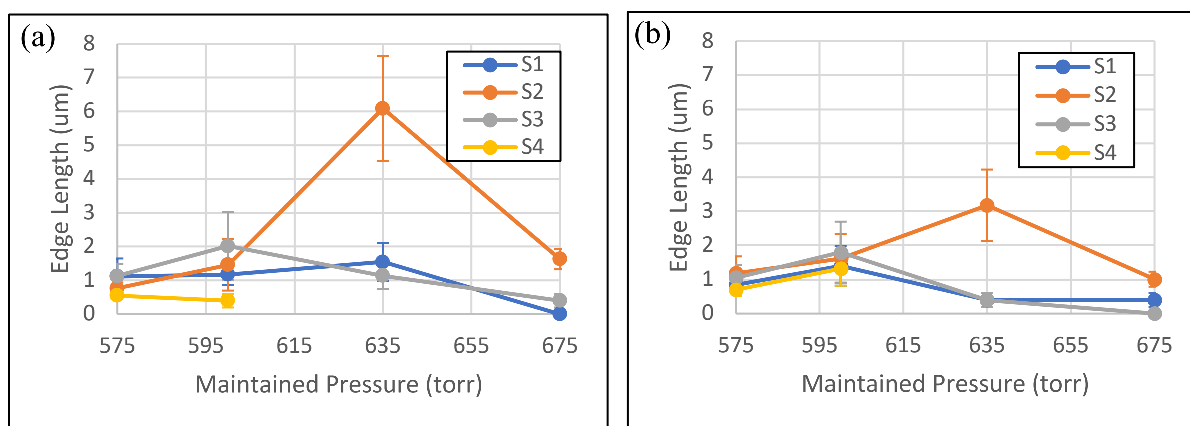

Figure 13: Plots of average particle edge length versus reaction pressures of $575, 600, 635,$ and $675\ torr$. (a) Left side of substrates (b) Right side of the Si/SiO_2 substrates. There was only a fourth substrate for the 575 and $600\ torr$ trials. Error bars are one standard deviation from N=100 measurements. Substrates S1, S2, S3, and S4 represent downstream distances relative to the MoO_3 precursor centered around distances of ~1.2, ~2.5, ~3.3, and ~4.8 cm respectively.

Figure 13 shows that the largest particle edge lengths were observed at the atmospheric pressure of 635 torr. The substrate that was centered 2.2 cm 1.4-3.0 cm downstream from the MoO_3 precursor contained the largest average particle edge lengths of 6.09 ± 1.55 µm on the left side of the substrate and 3.18 ± 1.05 µm on the right side. The largest isolated monolater triangle had an edge length of ~9.5 µm. This downstream distance range yielded the largest average growth due to the vapor precursor ratio discussed in Chapter 2.5.

The 675 torr sample showed only upstream and downstream edge triangle growth and no triangles larger than ~2.0 µm. We observed some triangular and hexagonal MoS_2 morphologies outside of the boat. This growth pattern could be due to the flow dynamics of the CVD system, or that the cleaved edges provide nucleation sites for particle growth **[38]**. The data in Figure 13 agrees with our hypothesis that reducing the maintained pressure to an atmospheric pressure of ~635 torr would yield the largest monolayer triangle edge length. This is consistent with APCVD literature **[37]**.

2.7 Maximum holding temperature

The reaction temperature influences particle edge length and morphology of monolayer growth **[39]**. We hypothesized that increasing the maximum holding temperature would increase the vapor pressure of the precursors, and increase the growth rate. Hence, we performed reactions at fixed separation distance and pressure, but varied the temperature over the range of 795, 800, and 810 °C (Figure 14), corresponding to temperature around the melting point of MoO_3 (795 °C). Temperatures further below the MoO_3 melting point were not investigated.

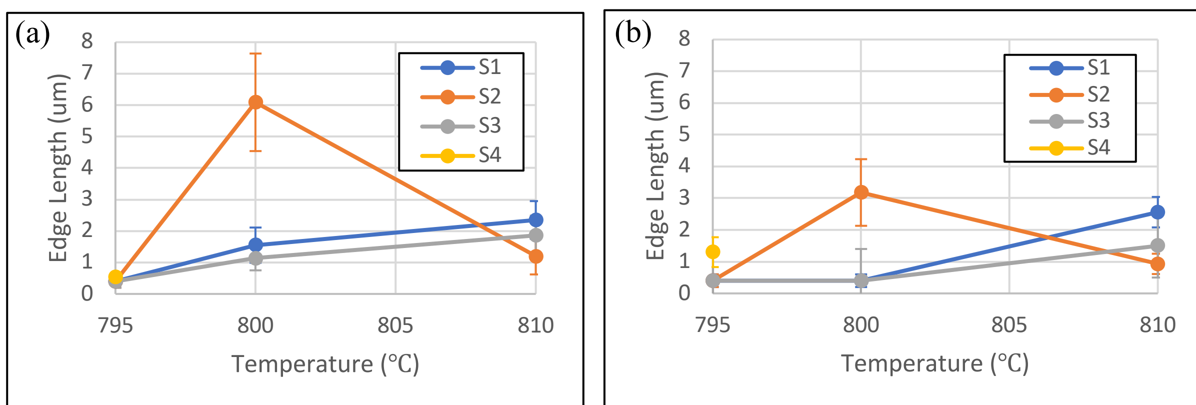

Figure 14: Plots of temperature versus particle edge length for the (a) left side of the substrate average triangle side length for the holding temperature experiments at 795, 800, and 810 ℃. The different substrate positions (S1, S2, S3, and S4) are represented by the different colored lines. (b) Right side of the substrate triangle lengths. There was only a fourth substrate for the 795 ℃ reaction, and error bars are one standard deviation for N=100 measurements. Substrates S1, S2, S3, and S4 represent downstream distances relative to the MoO_3 precursor centered around distances of ~1.0, ~2.5, ~3.7, and ~4.8 cm respectively.

Figure 14 shows that the largest triangular particle growth was observed at 800 °C, for the substrate that was placed 2.3 cm downstream from the MoO_3 precursor. The average triangle size for N=100 measurements, was 6.09±1.55 μm for the left side of the substrate, and 3.18 ± 1.05 μm for the right side. An increase of the average edge length was observed for the 810 °C trial on substrates ~1.0 and ~2.5 cm downstream from the MoO_3 precursor. This may indicate that the reaction location and MoS_2 growth has moved further downstream or outside of the boat. The edge length data from Figure 14 did not increase with temperature the way we had hypothesized. Higher temperatures may lead to a high molybdenum vapor pressure, promoting multi-layer growth rather than monolayer MoS_2.

2.8 Optimizing carrier gas flow rate

Having optimized the separation distance, pressure, and temperature, we studied the effect of carrier gas flow rate on MoS_2 edge length and morphology. The inert gas transports the vaporized sulfur down the reaction tube where it is able to react with the vaporized MoO_3. The growth on the substrates presumably exhibits Laminar flow dynamics, where the vapor in the center of the tube travels faster than the vapor at the sides (Figure 10a) **[40]**. This leads to the more densely covered center of the substrate, and the less densely covered MoS_2 growth regions. We hypothesized that using a high flow rate may move the reaction further down the tube, resulting in fewer observed MoS_2 monolayers. We alternatively hypothesized that a slow flow rate, there would not be enough sulfur vapor present at the substrates, also resulting in limited monolayer growth. A flow rate range of 50, 100, and 200 sccm (Figure 15) was selected around the initial flow rate known to yield monolayer growth, as discussed in Experimental Section 2.2.

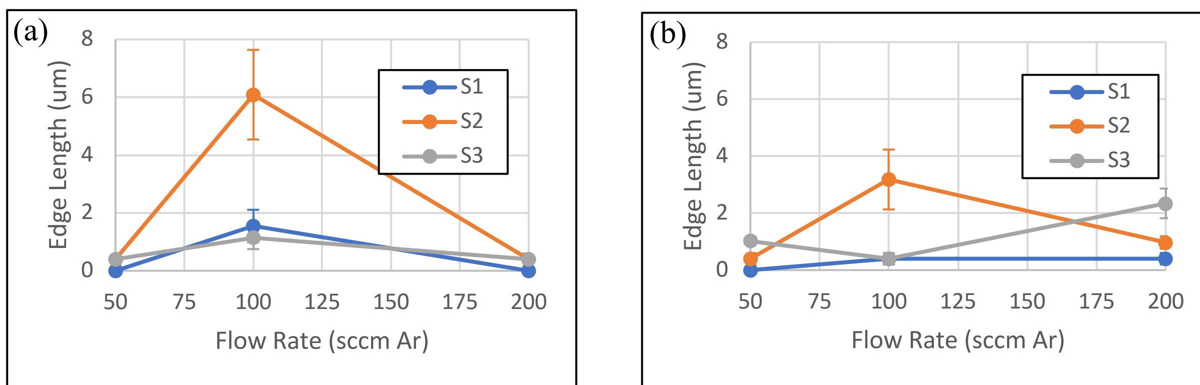

Figure 15: Plot of flow rate of the inert argon carrier gas versus particle edge length at 50, 100, and 200 $sccm$. (a) Left side and (b) right side of substrates. Error bars are one standard deviation from N=100 measurements. Substrates S1, S2, and S3 represent downstream distances relative to the MoO_3 precursor centered around distances of ~1.0, ~2.4, and ~4.3 cm respectively.

The data in Figure 15 shows a clear increase in particle edge length for the 100 sccm flow rate. Monolayer growth was observed the length of the substrates, with the largest particles ~2.4 cm downstream from the MoO_3 precursor. Triangles with edge lengths ≥ 9.5 µm were observed. Figure 15b shows a decrease in particle edge length for downstream substrate distances of ~1.0 and ~4.3 cm, most likely due to a surface defect (scratch or foreign object) on the substrate. This demonstrates the importance of thoroughly cleaning the substrates before the reaction, as discussed in Experimental Section 2.2.

There was increase in edge length for the 200 sccm flow rate at substrate distances 4.2 cm downstream from the MoO_3 (Figure 15b). This would agree with the hypothesis that the reaction is being moved further down the tube. This could be checked by adding additional substrates and extending the investigation area further downstream. The 50 sccm flow rate failed to yield edge lengths larger than ~1.5 µm agreeing with the hypothesis that not enough sulfur vapor was present to increase edge length.

2.9 Optimizing reaction hold time

The reaction duration or hold time is expected to influence particle edge length **[41]**. We hypothesized that increasing the hold time would increase the edge lengths of the monolayer MoS_2. At shorter holding times complete sulfurization of the molybdenum precursor may not occur, leading to dense multi-layer growth **[42]**. Hence, we varied the reaction hold time over the range of 10, 15, and 20 minutes to investigate the effect of reaction hold time versus particle edge length (Figure 16).

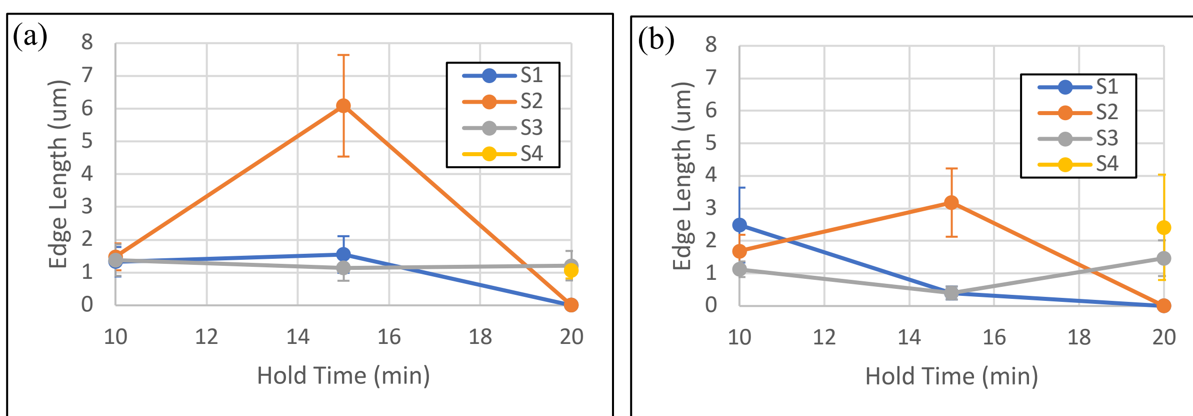

Figure 16: Plots of holding time versus particle edge length. Durations of 10, 15, and 20 minutes were the examined hold times at the maximum temperature 800 ℃. (a) Left side of growth substrates and (b) right side of growth substrates. Error bars are one standard deviation from N=100 measurements. Substrates S1, S2, S3, and S4 represent downstream distances relative to the MoO_3 precursor centered around distances of ~1.0, ~2.4, ~4.3, and cm respectively.

Figure 16 shows the particle edge length versus reaction holding time. The largest particle growth was observed at the 15-minute holding time on substrate 2, which corresponds to 2.25 cm downstream from the MoO_3 precursor. The average triangle growth size from substrate 2 being 6.09 ± 1.55 µm on the left side, and 3.18 ± 1.05 µm on the right side of the substrate. A holding time of 10 minutes produced a larger quantity of triangles, but much smaller edge lengths ~1.13-2.49 µm, with the majority of the triangles being less than 0.4 µm in size.

At a holding time of 20-minutes and for substrates that were placed 0.5-3.25 cm downstream from the MoO_3 precursor, triangle growth did not occur on the substrate inside the boat. There were however, sub 0.4 μm triangles observed on the outside edges of the substrates. Substrates at distances 3.3-5.5 cm downstream showed lager particle growth at the 20-minute holding time, but triangles on average were not as large as the 15-minute hold time. The data in Figure 16 disagrees with our hypothesis that longer holding times would increase edge length. Particles would not decrease in edge length once they reached the edge lengths seen at a 15-minute hold time. This implies that the larger particle growth may have moved further downstream or outside of the boat. Also, by averaging the edge lengths, the abundance of smaller triangles may skew the data. It is also the possible that longer holding times increase the multi-layer growth, or merging of triangles into films.

CHAPTER 3: SPECTROSCOPIC CHARACTERIZATION OF CVD-GROWN MoS_2

Having determined the optimal growth conditions that maximize the edge length of equilateral MoS_2 triangles, we used photoluminescence (PL) and Raman micro-spectroscopy to characterize the sample composition and layer thickness. The optical microscopy data in Chapter 2 assumed that the equilateral triangles were consistent with ML-MoS_2 growth, in agreement with literature **[43]**. In a typical experiment, we used a ~5.4 cm by ~2.0 cm Si/SiO_2 substrate and the following growth conditions in Table 1.

Table 1: Optimal MoS_2 monolayer CVD growth conditions and precursor quantities

MoO_3 precursor amount (mg)	Sulfur precursor amount (mg)	Precursor separation distance (*cm*)	Maintained pressure (*torr*)	Maximum temperature (° *C*)	Carrier gas flow rate (*sccm*)	Reaction hold time (*min*)
2.0	10.0	15	635	800	150	15

3.1 CVD growth on large Si/SiO_2 substrates for spectroscopic characterization

Figure 17 shows an optical micrograph of the large Si/SiO_2 substrate (~200 nm oxide layer thickness) before and after the CVD reaction parameters shown in Table 1.

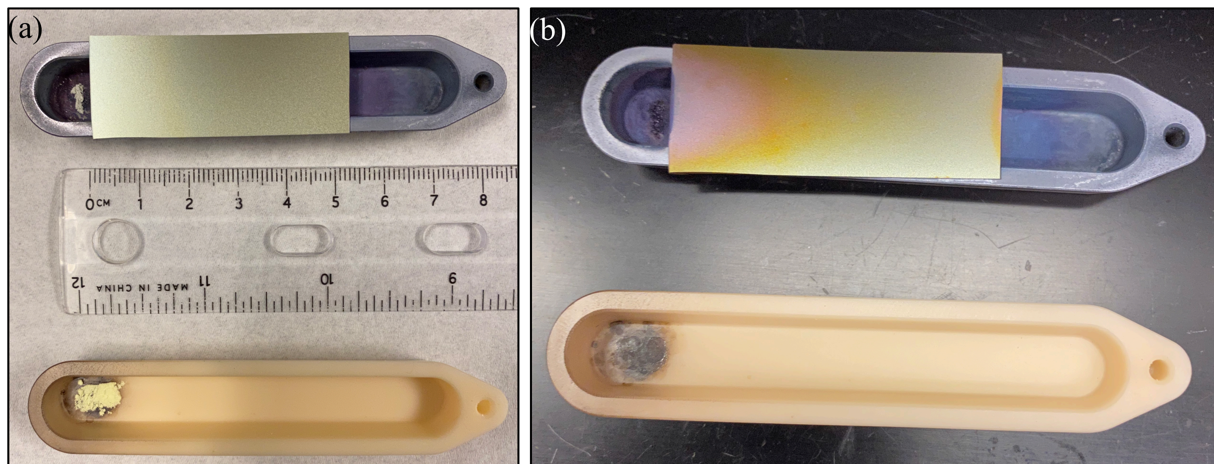

Figure 17: Optical micrograph of longer (5.4 cm) Si/SiO_2 substrate (a) before reaction, and (b) post reaction using reaction conditions from Table 1. Ruler used to spatially align the optical microscope images with their physical location on the substrate.

The substrates have the thermal oxide layer facing down and placed alongside a ruler to align the particle measurements from the optical images with their physical location on the substrate. Post CVD reaction (Figure 17b), the non-oxide layer side of the substrate shows similar coloration and Laminar flow front as seen on the oxide layer side, but no MoS_2 triangle growth was observed on the Si side.

Figure 18a shows a photograph of the thermal oxide side of the longer Si/SiO_2 substrate after CVD-growth. Figure 18b-c shows the average triangle edge length versus distance for both left and right sides of the substrate.

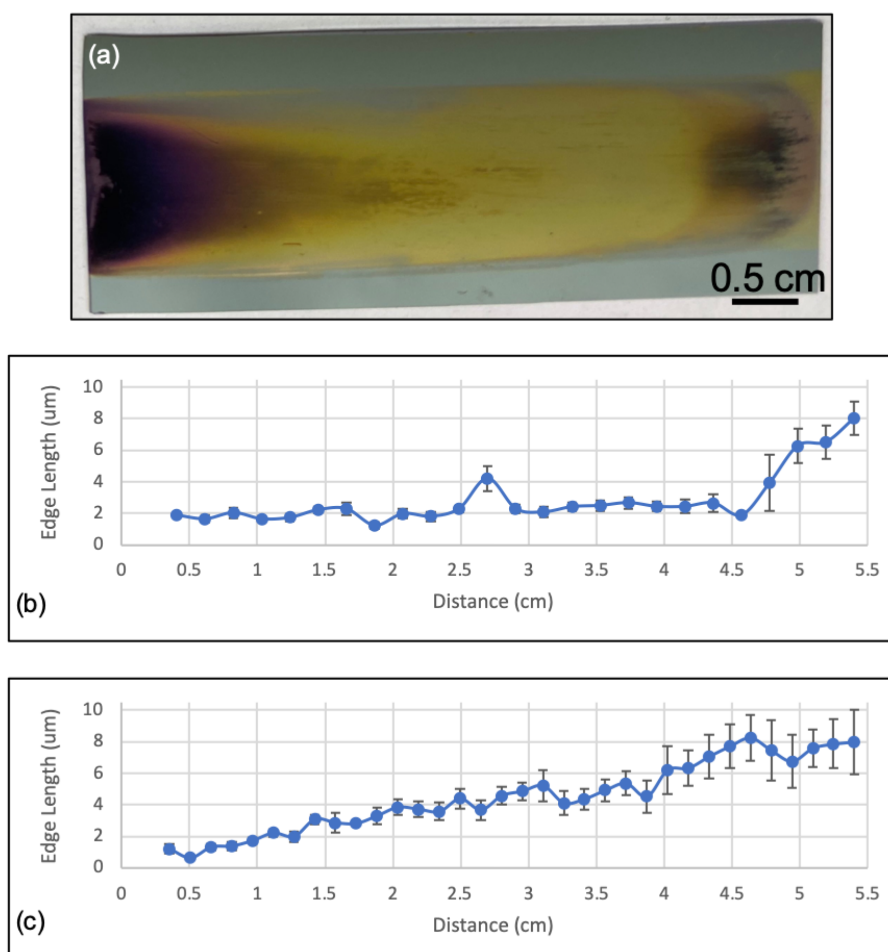

Figure 18: Combination of the single variable experiments to optimize MoS_2 triangle growth size. (a) Photograph of thermal oxide side of growth substrate after a CVD reaction. The Si/SiO_2 substrate was placed ~0.5-5.9 cm upstream from MoO_3 precursor. Corresponding plots of distance relative to the MoO_3 precursor versus particle edge length for the left (b) and right (c) sides of the substrate. Error bars are one standard deviation for N=15 ± 5 measurements.

The error bars are one standard deviation from N=15 ± 5 measurements at each distance. The monolayer MoS_2 triangles increased in edge length as the distance from the MoO_3 precursor increased (Figure 18b and 18c). The largest isolated monolayer MoS_2 triangles exceeded edge lengths of ~11μm. The CVD reaction using the optimal growth conditions from Table 1 and a longer ~5.4 cm substrate was repeated three times to confirm that the results in Figure 18 were reproducible.

Figure 19 shows an optical micrograph of some of the largest isolated monolayer MoS_2 from the sample in Figure 18. These large equilateral triangles were observed ~4.7 cm downstream from the MoO_3 precursor on the left side of the Si/SiO_2 substrate. Possible larger edge lengths were seen, but the triangles merged into films and were no longer isolated. Some bilayer growth was seen at the center of some of the equilateral triangles.

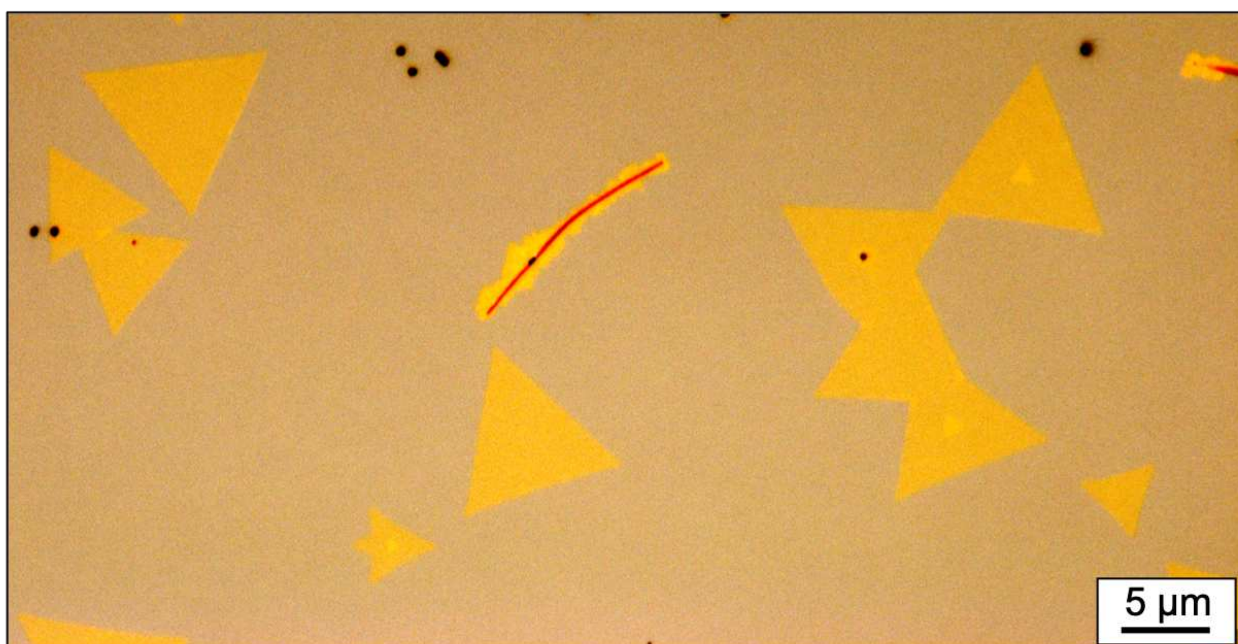

Figure 19: Optical microscope image of some large monolayer MoS_2 growth from the experimentally determined growth conditions from Table 1. The triangles were located ~4.7 cm downstream from the MoO_3 precursor. The Si/SiO_2 substrate had an oxide layer of ~200 nm thick.

3.2 Raman spectroscopy

PL and Raman micro-spectroscopy measurements were performed on an inverted Olympus IX73 microscope. A 532 nm laser (Ondax-THz Raman system) passes through a 100x (Olympus PlanFL N100X NA 0.95) objective and excites a ~690 nm diameter spot on the sample. The signals are sent back through the 100x objective and filtered by the Ondax-THz Raman system. The signal is then passed through a Horiba iHR 550 spectrometer and detected by a back illuminated charge coupled device (Synapse CCD) detector **[44]**. The excitation power used for the 532 nm Raman excitation was 120 mW, with acquisition times between 5-20 seconds.

The MoS_2 layer thickness can be determined from Raman spectroscopy measurements **[45]**. Specifically, the peak separation between the E_{2g}^{1} and A_{1g} modes depends on the layer thickness. These MoS_2 fingerprint peaks appear at ~380 (E_{2g}^{1}) and ~400 cm^{-1} (A_{1g}). Both peaks move as layer number increases, with the E_{2g}^{1} peak (inter-plane vibrational mode) moving to lower energy wavenumbers and the A_{1g} peak (intra-plane vibrational mode) moving to higher energy wavenumbers **[46]**.

Figure 20a shows an optical reflection image of an MoS_2 triangle. There are two smaller triangles that grew in the center of the large triangle. These smaller triangles likely represent bilayer and trilayer-thick material, in agreement with literature **[47]**. Figure 20b shows a representative Raman spectrum from the blue and orange circle regions in Figure 20a. The fitted spectral data shows the two fingerprint peaks located at ~375 and 395 cm^{-1}. The peaks from the assumed monolayer region (orange line) appear at 374.2 and 395.2 cm^{-1}, showing a smaller peak separation of 21.0 cm^{-1} consistent with monolayer peak separation. The peaks from the assumed bi or tri-layer thick MoS_2 region appeared at 373.1 and 396.5 cm^{-1}, with a peak separation of 23.4 cm^{-1}, in agreement with trilayer-thick multilayer growth. The peak intensities were larger for the

multi-layer region and the A_{1g} peak counts were larger in comparison to the smaller E_{2g}^1 peak. The peak intensities and peak separations were determined from Lorentzian fits. Next, we raster scanned the laser across the sample to obtain peak intensity as a function of laser excitation position data. At each laser position a spectrum was taken and can be correlated with Figure 20a. Panel 20c shows the selected laser positions to plot the peak separation data seen in Figure 20d. The resolution of the Raman peak intensity map is limited by the laser spot size (690 nm).

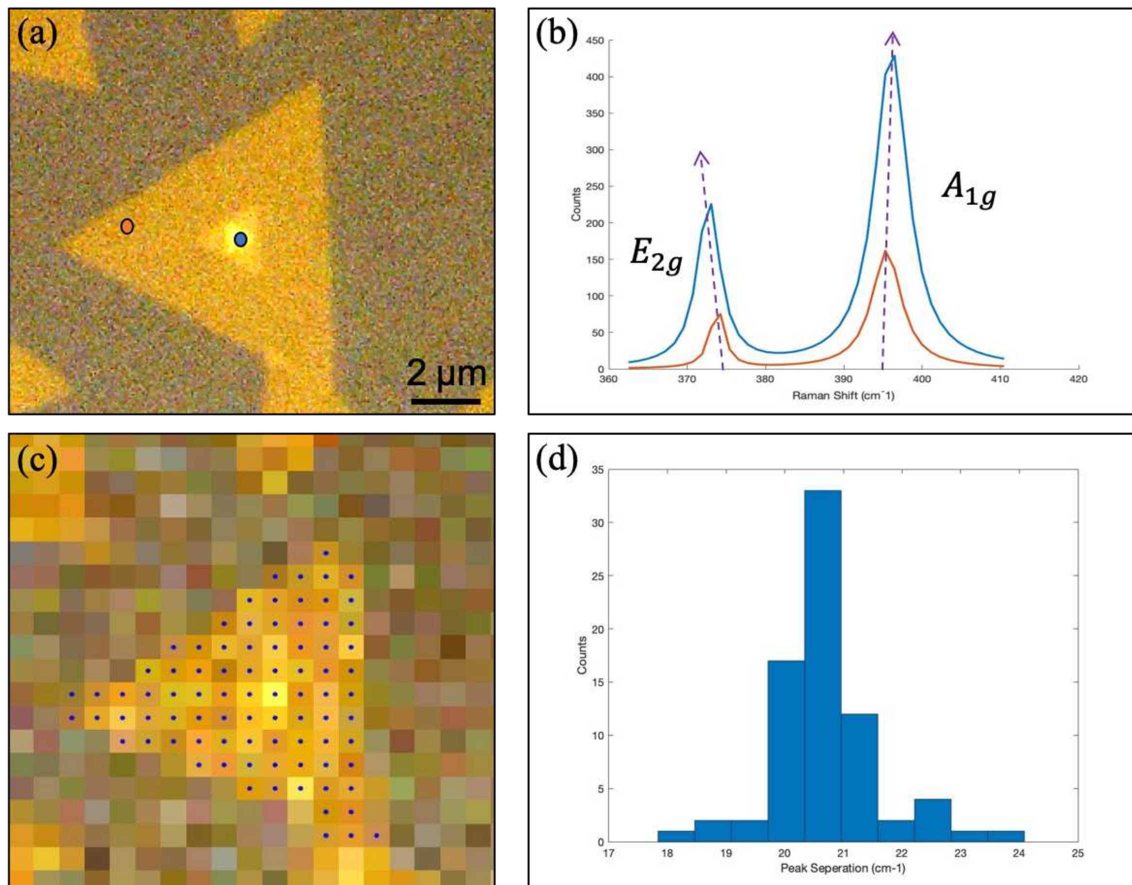

Figure 20: (a) Cropped optical image of single triangle with bi and tri-layer growth seen in the center. Monolayer (orange circle) and multi-layer region (blue circle) where individual spectra were taken. (b) Representative Raman spectrum from the blue and orange circle regions in panel a. Arrowed lines added to demonstrate the peak separation as layer thickness increases. (c) Selected laser positions to plot the peak separation data seen in (d) distribution of peak separation. A 532 nm laser excited the MoS_2 triangle, with power of 120 mW.

Figure 20d shows the distribution of Raman peak separations from all of the spectra in Figure 20c. A large population appears at 20-21 cm^{-1} and a small population appears ~22.5 cm^{-1}. These populations can be attributed to monolayer (1L) and bi-layer (2L), MoS_2 whose peak separations are expected to be ~18.0-21.3 and 22.4 cm^{-1}, respectively **[48]**. Trilayer (3L)-thick MoS_2 is expected to appear at 23.5 cm^{-1}. There is some indication in optical reflection data that 3L-thick material exists at the center of MoS_2 triangles (Figure 20a), but there is only one spectral data point at these locations and the laser spot size is much larger than the feature size, which obscures us from concluding whether the largest peak separation data is due to 3L-thick MoS_2. From the data analysis distribution, these results correlate nicely with qualitative optical image, as well as the expected peak separation distances. In summary, Raman spectroscopy measurements indicate that these samples are MoS_2 and the peak-to-peak separations are consistent with monolayer and bilayer-thick material.

3.3 Photoluminescence spectroscopy

The same microscope set up was used for photoluminescence measurements, but with a 415 nm laser being used for the excitation source. Powers of 10-25 mW, and acquisition times between 2-20 seconds were used to obtain the PL spectra. The 415 nm laser was chosen because it is in resonance with the C-exciton states of 1L-MoS_2 and is absorbed more than the 532 nm laser light. PL measurements have shown the PL peak position and intensity is sensitive to layer thickness. Bulk, 3L, and 2L MoS_2 have indirect bandgaps of 1.23, 1.46, and 1.59 eV, and 1L-MoS_2 has a direct bandgap of 1.80-1.89 eV **[49]**. Hence, photoluminescence spectroscopy was used to confirm that the radiative emission from the MoS_2 triangles was due to the expected direct bandgap transition of 1L-MoS_2.

Figure 21b shows a representative PL spectrum from the blue and orange circled regions on the MoS_2 triangle shown in Figure 20a. The raw data was fit with a Gaussian function to extract the PL intensity peak wavelength. The wavelength in units of nm was converted to units of eV according to Eq. 1,

$$Eq. 1: E(eV) = \frac{hc}{\lambda}$$

where c is the speed of light ($3x10^8$ m/s), h is Plank's constant ($6.64x10^{-34}$ J·s), and then converting Joules to electron volts (eV), 1 eV = $1.60x10^{-19}$ J. The spectrum in Figure 20b shows a strong PL peak at 667.7 nm, corresponding to 1.86 eV, which agrees with the direct bandgap energy of 1L-MoS_2 (1.80-1.89 eV) **[49]**. The direct bandgap transition is also apparent by comparing the intensities between the two spectral regions. The monolayer MoS_2 has an integrated peak intensity an order of magnitude larger than the assumed multi-layer region. The multi-layer PL peak center also shifts to lower energy wavelengths.

To further characterize the layer thickness of these samples, we mapped the PL peak intensity of a large sample area (Figure 21a). The acquisition time per pixel was 20 s and the laser power used was 10 mW. The spatial resolution of the PL maps is limited by the spot size of the laser. Figure 21c shows the PL map of the region in Figure 21a. The PL intensity data represents the integrated area under the PL peak. The photoluminescence intensity map demonstrates that many triangles in the sample exhibit thickness-dependent intensities as the single triangle in Figure 20. 1L-MoS_2 regions appear as dark red pixels in the map due to the intense direct bandgap emission whereas the 2L or 3L-thick regions appear as blue pixels due to the weak indirect bandgap transition. Additionally, the edges of triangles show a lower intensity than expected for monolayers. This is likely due to the laser spot exciting a much larger area than the sample edge. In this scenario, the laser excites both the MoS_2 triangle and the Si/SiO_2 substrate.

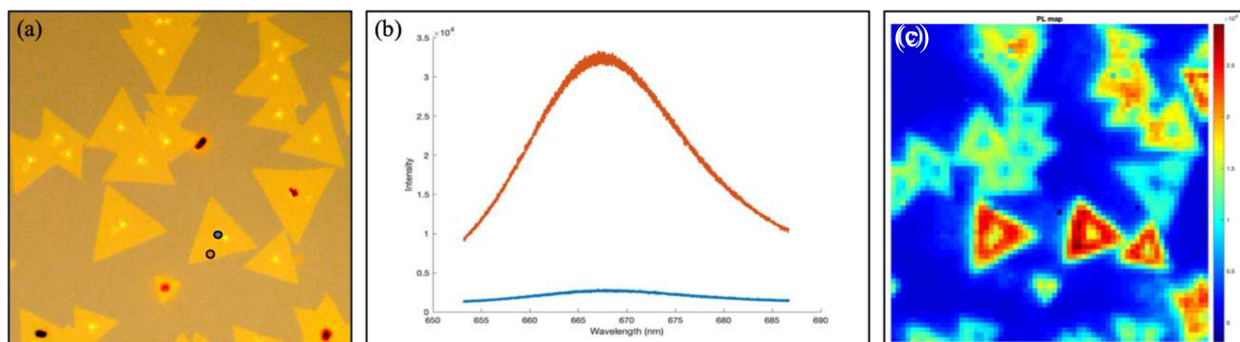

Figure 21: (a) Cropped, optical microscope image of triangle growth region at 100x magnification. The blue and orange dots represent where the PL spectrua in panel b were acquired. (b) Gaussian fit spectral data for the spectra indicated in panel a, with a monolayer peak center at 667.7 nm (1.86 eV). (c) PL map of the same triangular growth region with 100x objective, 10 mW laser power, and 20 second acquisition time.

3.4 Correlating PL intensity and Raman peak shifts for layer-thickness characterization

By plotting the layer thickness dependent photoluminescence intensity versus Raman shift peak separation, it was expected that 1L-thick MoS_2 would exhibit high PL and small Raman peak separation (~18-21 cm^{-1}). Bilayers would have a dramatic decrease in PL intensity, due to the indirect bandgap, as well as a slight increase in Raman shift fingerprint peak separation, ~22.4 cm^{-1}. Following that trend, the 3L would have an even lower PL intensity as well as a broader Raman peak separation of ~23.3 cm^{-1}.

To plot the PL intensity versus Raman peak separation for individual triangles, we developed a MATLAB image processing routine to quantitatively overlay photoluminescence and Raman maps. First, the Raman spectral data from each pixel was fit with Lorentzian fits for the fingerprint A_{1g} and E_{2g} peaks in each spectrum. The curve fitted peak separations were measured and those smaller than 17 cm^{-1} and greater than 26 cm^{-1} were excluded because they do not represent 1L, 2L, or 3L-thick MoS_2. To correlate and align the optical image with the Raman and PL maps, the optical image is first transformed to match the lower resolution PL map. Four position markers were selected in each image (such as center points or corners of MoS_2 triangles) and the same four points were selected in the PL map. The MATLAB code converts and realigns the

optical image to match that of the PL and Raman maps. The Raman map was correlated in the same manner by selecting four points on the PL map and selecting the same points in the Raman map (Figure 22).

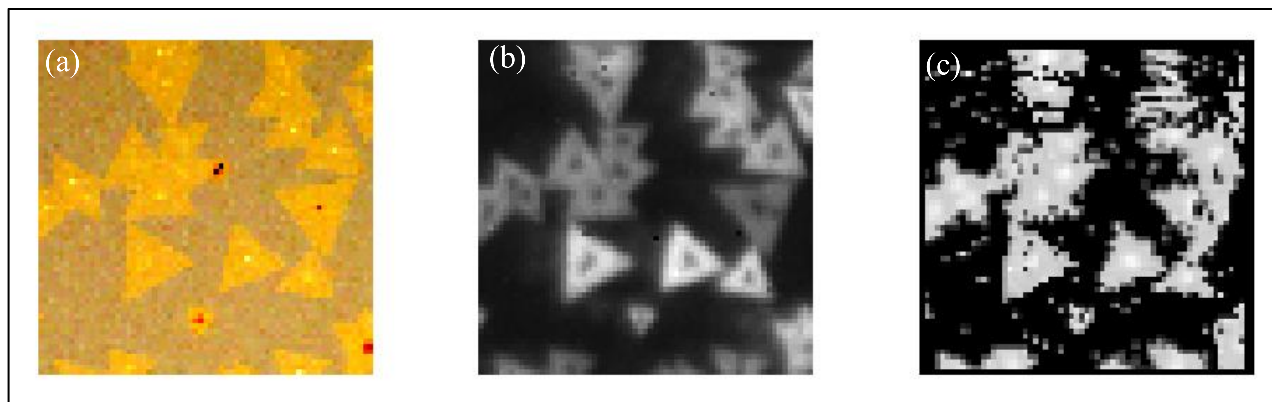

Figure 22: (a) Optical image of triangular growth region converted to pixels for correlation to PL and Raman shift maps. (b) Correlated photoluminescence intensity map of triangular MoS_2 growth region. (c) Raman shift, A_{1g} and E_{2g}^{1}, peak separation map.

Once the optical image and spectral maps were aligned, pixels on the converted optical image were selected based on their apparent layer thickness seen in the optical image (Figure 21a). The selected 1L, 2L, and 3L pixels produce the xy data for a PL versus Raman shift plot (Figure 23). These data points represent values from specifically selected individual spectra that qualitatively appeared to represent 1L, 2L, and 3L-thick MoS_2 seen in Figure 19a. As expected, there was dramatic decrease in integrated PL intensity observed when layer thickness increases from single to bilayer. This data further confirms the successful CVD growth of monolayer MoS_2.

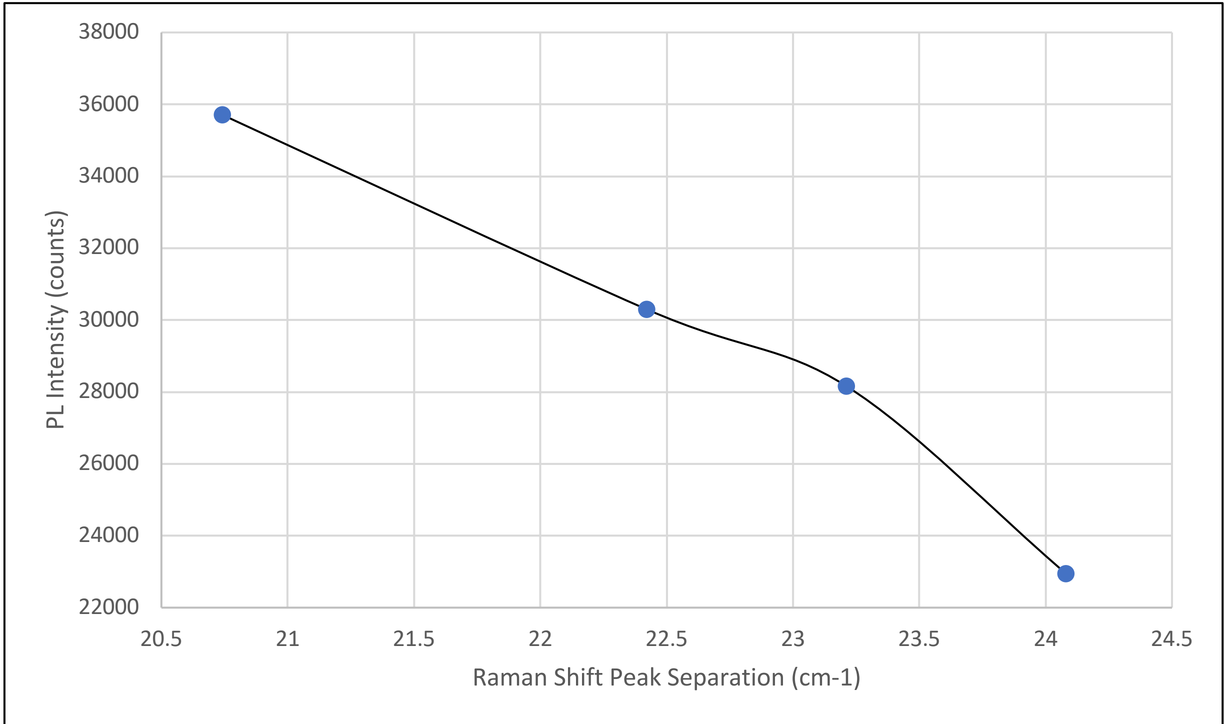

Figure 23: Plot of the integrated PL intensity versus Raman Shift peak separation for individually selected spectra. At smaller peak separations the PL intensity is high due to the direct bandgap transition of monolayer MoS_2. As layer thickness increases PL intensity drops due to the indirect bandgap transition in 2L, 3L, and bulk crystal MoS_2.

CHAPTER 4: CONCLUSIONS AND DIRECTIONS FOR FURTHER OPTIMIZATION

The CVD synthesis of monolayer MoS_2 yielded reproducible equilateral triangular particles with edge lengths exceeding 11 μm. Through the series of single variable experiments, the equilateral triangle growth characteristic of monolayer, was optimized to increase edge length and control growth location on the Si/SiO_2 growth substrates. Maximum temperature, maintained pressure, carrier gas flow rate, holding time, and precursor separation distance were the experimental variables investigated. Some variables such as pressure and precursor separation distance had large effects on MoS_2 particle edge length and growth location. For the investigated reaction conditions, other variables such as temperature and flow rate appeared to have less of an effect on the monolayer MoS_2 edge length. Layer thickness was first assumed based off of equilateral triangle morphology and confirmed through Raman and PL spectral analysis. The data showed the successful reproducible CVD growth of monolayer MoS_2 materials, but further optimization is still necessary.

One interesting future direction would be to investigate the different MoS_2 morphologies seen from the CVD growth. Along with equilateral triangle MoS_2 morphologies, indented/pinched, curved, and rounded corner triangles were also seen on the growth substrates. In addition, there were hexagons, and transition morphologies seen between triangles and hexagons (Figure 24). Some of these morphologies result from different edge termination. Equilateral triangles are known to have sulfur terminated edges, where hexagonal morphologies have alternating sulfur and molybdenum terminated edges **[50]**. These different morphologies and edge terminations can be used to further study the effect of edge sites on charge carrier separation and transport in monolayer MoS_2.

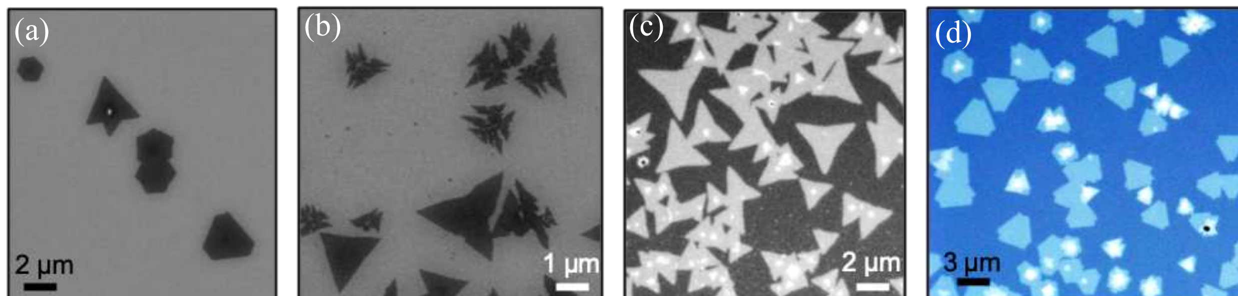

Figure 24: Images of different MoS_2 monolayer growth morphologies. (a-b) SEM images of hexagonal and fractal morphologies. (c-d) Optical reflection images of pinched triangles and transition morphologies.

Another direction of optimization could focus on the surface defects in the monolayer MoS_2. The surface of the CVD grown MoS_2 is also known to have sulfur atom vacancies. These could be addressed by increasing the sulfur precursor amount in order to reduce the amount of surface defects, or alternatively, dope the material. Doping of TMDs has been shown to increase the material's conductivity **[51]**. There is also a large amount of unwanted growth in the center of the substrates. These unwanted particles are also observed on top of MoS_2 triangles and merged films. This could possibly be reduced or removed by reducing the amount of MoO_3 precursor used thereby increasing the sulfur to molybdenum vapor precursor ratio. This would hopefully result in more substrate surface area coverage and possibly much larger monolayer particle growth. Additionally, investigating temperatures below the melting point of the MoO_3 may lead to less dense coverage in the center of the substrate, allowing for more, or larger particle growth. Other variables, such as maintained pressure and holding time, might have to also be adjusted simultaneously to compensate for the lower temperature. The continued optimization of monolayer MoS_2 can be pursued through these possible avenues.

Through the series of optimization experiments (maximum temperature, maintained pressure, carrier gas flow rate, holding time, and precursor separation distance), triangular MoS_2 morphology was observed, and monolayer growth was confirmed via spectroscopy. Raman

spectroscopy data showed an average monolayer peak separation of 18-21 cm^{-1} consistent with literature. The photoluminescence spectroscopy showed the monolayer direct bandgap energy of 1.86 eV, and a much larger peak intensity compared to 2L or 3L-thick MoS_2. The location of particle growth was able to be moved from initially outside of the alumina boats, to inside the boat, by decreasing the precursor separation distance from 16.0 to 15.0 cm. Using a single, longer Si/SiO_2 growth substrate, showed more consistent and larger particle growth than the smaller individually cut ones. The particle edge length was also seen to increase, by an order of magnitude, due to the adjustment to an atmospheric pressure of ~635 torr as well as precursor separation distance. Isolated triangular morphologies were observed at sizes in excess of 11 μm. Being able to consistently synthesize these materials, and control specific properties (size and morphology) will aid in the further fundamental investigation of electrochemical, optical, and electrical properties of monolayer MoS_2.

REFERENCES

[1] Novoselov, K. S.; Fal′ko, V. I.; Colombo, L.; Gellert, P. R.; Schwab, M. G.; Kim, K. A Roadmap for Graphene. *Nature.* **2012**, *490*(7419), 192–200.

[2] Velický, M.; Toth, P. S. From Two-Dimensional Materials to Their Heterostructures: An Electrochemists Perspective. *Applied Materials Today.* **2017**, *8*, 68–103.

[3] Novoselov, K. S.; Jiang, D.; Schedin, F. Two-dimensional atomic crystals. *Proc. Natl. Acad. Sci. U.S.A.* **2005**, *102*, 10451-10453.

[4] Bolotin, K.; Sikes, K.; Jiang, Z.; Klima, M. Ultrahigh electron mobility in suspended graphene. *Solid State Communications.* **2008**, *146*, 351-355.

[5] Bernardi, M.; Palummo, M.; Grossman, J.C. Extraordinary sunlight absorption and one nanometer thick photovoltaics using two-dimensional monolayer materials. *Nano Lett.* **2013**, *13*, 3664-3670.

[6] Chhowalla, M.; Shin, H.S.; Eda, G.; Li, L.J.; Loh, K.P.; Zhang, H. The chemistry of two-dimensional layered transition metal dichalcogenide nanosheets. *Nat. Chem.* **2013,** *5*, 263-275.

[7] Tonndorf, P.; Schmidt, R.; Bottger, P.; Zhang, X. Photoluminescence emission and Raman response of monolayer MoS_2, $MoSe_2$, and WSe_2. *Opt. Express*. **2013**, *21,* 4908-4916.

[8] Wilson, J.; Yoffe, A. The Transition Metal Dichalcogenides Discussion and Interpretation of the Observed Optical, Electrical and Structural Properties. *Advances in Physics.* **1969**, *18*(73), 193–335.

[9] Kappera, R.; Voiry, D.; Yalcin, S.E.; Branch, B.; Gupta, G. Phase-engineered low-resistance contacts for ultrathin MoS_2 transistors. *Nat. Mater.* **2014**, *13,* 1128-1134.

[10] Mak, K.F.; Lee, C.; Hone, J.; Shan, J. Atomically thin MoS_2: a new direct-gap semiconductor. *Phys. Rev. Lett.* **2010**, *105,* 136805.

[11] Frindt, R.F.; Yoffe, A.D. Physical Properties of Layer Structures: Optical Properties and Photoconductivity of Thin Crystals of Molybdenum Disulfide. *Proceedings of the Royal Society of London. Series A. Mathematical and Physical Sciences.* **1963**, *273*(1352), 69–83.

[12] Frindt, R.F. Single crystals of MoS_2 several molecular layers thick. *J. Appl. Phys.* **1966**, *37*, 1928-1929.

[13] Jeon, J.; Jang, S.K.; Jeon, S.M. Layer-controlled CVD growth of large-area two-dimensional MoS_2 films. *Nanoscale.* **2015**, *7,* 1688-1695.

[14] Zheng, J.; Zhang, H.; Dong, S.; Liu, Y. High yield exfoliation of two-dimensional chalcogenides using sodium naphthalenide. *Nat. Commun.* **2014**, *5*, 2995.

[15] Santiago, Y.; Cabrera, C.R. Surface analysis and electrochemistry of MoS_2 thin films prepared by intercalation-exfoliation techniques. *J. Electrochem. Soc.* **1994**, *141*, 629-635.

[16] Zeng, Z.; Yin, Z.; Huang, X.; Li, H. Single-layer semiconducting nanosheets: high-yield preparation and device fabrication. *Angew. Chem. Int. Ed.* **2011,** *50*, 11093-11097.

[17] Brixner, L.H. Preparation and properties of the single crystalline AB2-type selenides and tellurides of niobium, tantalum, molybdenum, and tungsten. *J. Inorg. Nucl. Chem.* **1962,** *24*, 257-263.

[18] Kline, G.; Kam, K.; Canfield, D. Efficient and stable photoelectrochemical cells constructed with WSe_2 and $MoSe_2$ photoanodes. *Sol. Energy Mater.* **1981**, *4*, 301-308.

[19] Butler, S.Z.; Hollen, S.M.; Cao, L.; Cui, Y.; Gupta, J.A. Progress, challenges, and opportunities in two-dimensional materials beyond graphene. *ACS Nano.* **2013**, *7,* 2898-2926.

[20] Shaw, J. C.; Zhou, H.; Chen, Y.; Weiss, N. O.; Liu, Y.; Huang, Y.; Duan, X. Chemical vapor deposition growth of monolayer MoSe2 nanosheets. *Nano Research* **2014**, *7*(4), 511–517.

[21] Lv, R.; Robinson, J.A.; Schaak, R.; Sun, D. Transition metal dichalcogenides and beyond: synthesis, properties, and applications of single- and few-layer nanosheets. *Acc. Chem. Res.* **2015**, *48*, 56-64.

[22] Gomathi, A.; Manna, A.K.; Late, D.J.; Datta, R. MoS_2 and WS_2 analogues of graphene. *Ang. Chem.* **2010**, *49(24)*, 4059-4062.

[23] Wang, S.; Rong, Y.; Fan, Y.; Pacios, M. Shape evolution of monolayer MoS_2 crystals grown by chemical vapor deposition. *Chem. of Mater.* **2014**, *26(22)*, 6371-6379.

[24] Sial, M.N.; Usman, M.; Zheng, B.; Mavric, A.; Qing, F. CVD growth of molybdenum diselenide surface structures with tailored morphology. *Cryst. Eng. Comm.* **2018**, *20*(33), 4867-4874.

[25] Hua, Y.; Wei, C.; Xuezeng, T.; Donghua, L. Scalable growth of high-quality polycrystalline MoS_2 monolayers on SiO_2 with tunable grain sizes. *ACS Nano.* **2014**, *8(6)*, 6024-6030.

[26] Liu, K. *et al.* Growth of large-area and highly crystalline MoS_2 thin layers on insulating substrates. *Nono Lett.* **2012**, *12*, 1538-1544.

[27] Zhan, Y.; Liu, Z.; Najmaei, S. Large-area vapor-phase growth and characterization of MoS_2 atomic layers on a $SiSiO_2$ substrate. *Small.* **2012**, *8*, 966-971.

[28] Ozden, A.; Ay, F.; Sevik, C. CVD growth of monolayer MoS_2: role of growth zone configuration and precursors ratio. *JJAP* **2017**, *56*, 06GG05 1-8.

[29] Lee, Y.H.; Zhang, X.Q.; Zhang, W.; Chang, M.T.; Lin, C.T. Synthesis of large-area MoS_2 atomic layers with chemical vapor deposition. *Adv. Mater.* **2012**, *24*, 2320-2325.

[30] Najmaei, S.; Lui, Z.; Zhou, W.; Zou, X.; Shi, G. Vapour phase growth and grain boundary structure of molybdenum disulfide atomic layers. *Nat. Mater.* **2013**, *12*, 754-759.

[31] Li, M.; Yao, J.; Wu, X.; Zhang, S. P-type doping in large area monolayer MoS_2 by chemical vapor deposition. *ACS Appl. Mater. Interfaces* **2020**, *12*, 6276-6282.

[32] University Wafer. Thermal oxide growth calculator. *University Wafer* **2019**. https://www.universitywafer.com/Oxide_Calculator/oxide_calculator.html

[33] BYU Cleanroom. Silicon dioxide/nitride color film thickness and viewing angle calculator. *Brigham Young University Electrical & Computer Engineering* **2019**. https://cleanroom.byu.edu/color_chart

[34] Van Der Zande, A.M.; Huang, P.Y.; Chenet, D.A. Grains and grain boundaries in highly crystalline monolayer molybdenum disulfide. *Nat. Mater.* **2013**, *12*, 554-561.

[35] Amani, M.; Chin, M; Mazzoni, A.L. Growth substrate induced performance degradation in chemically synthesized MoS_2 field effect transistors. *App. Phys. Lett.* **2014**, *104(20)*, 203506.

[36] Zhao, Y.; Lee, H.; Choi, W. Large-area synthesis of monolayer $MoSe_2$ films on Si/SiO_2 substrates by atmospheric pressure chemical vapor deposition. *RSC Advances* **2017**, *7(45)*, 27969-27973.

[37] Ionescu, R.; Wang, W.; Chai, Y. Synthesis of atomically thin MoS_2 triangles and hexagrams and their electrical transport properties. *IEEE Trans. on Nanotech.* **2014**, *13(4)*, 749-754.

[38] Menzel, A.; Goldberg, R.; Burshtein, G. Role of carrier gas flow and species diffusion in nanowire growth from thermal CVD. *J. Phys. Chem.* **2012**, *116(9)*, 5524-5530.

[39] Yang, S.Y.; Shim, G.W.; Seo, S.B. Effective shape-controlled growth of monolayer MoS_2 flakes by powder-based chemical vapor deposition. *Nano Research* **2017**, *10(1)*, 255-262.

[40] Kuwana, K.; Endo, H.; Saito, K. Catalyst deactivation in CVD synthesis of carbon nanotubes. *Carbon* **2005**, *43(2)*, 253-260.

[41] Yang, Y.; Fei, H.; Ruan, G. Edge-oriented MoS_2 nanoporous films as flexible electrodes for hydrogen evolution reactions and supercapacitor devices. *Adv. Mater.* **2014**, *26(48)*, 8163-8168.

[42] Zhu, D.; Shu, H.; Jiang, F. Capture the growth kinetics of CVD growth of two-dimensional MoS_2. *2D Mater. and Appl.* **2017**, *1*, 8.

[43] Xie, Y.; Wang, Z.; Zhan, Y. Controllable growth of monolayer MoS_2 by chemical vapor deposition via close MoO_2 precursor for electrical and optical applications. *Nanotechnology* **2017**, *28(8)*, 084001.

[44] Wang, L.; Nilsson, Z.; Sambur, J. Influence of the Substrate on the Optical and Photo-electrochemical Properties of Monolayer MoS_2. *ACS Appl. Mater. Interfaces* **2020**, *12*(13), 15034-15042

[45] Chakraborty, B.; Matte, H.S.S.; Sood, A.K. Layer-dependent resonant Raman scattering of a few layer MoS_2. *J. of Raman Spec.* **2013**, *44(1)*, 92-96.

[46] Najmaei, S.; Liu, Z.; Ajayan, P.M. Thermal effects on the characteristic Raman spectrum of molybdenum disulfide (MoS_2) of varying thickness. *Appl. Phys. Lett.* **2012**, *100*, 013106.

[47] Park, J.; Choudhary, N.; Smith, J. Thickness modulated MoS_2 grown by chemical vapor deposition for transparent and flexible electronic devices. *Appl. Phys. Lett.* **2015**, *106*, 012104.

[48] Li, H.; Zhang, Q.; Yap, C. C. R.; Tay, B. K.; Edwin, T. H. T.; Olivier, A.; Baillargeat, D. From Bulk to Monolayer MoS2: Evolution of Raman Scattering. *Advanced Functional Materials* **2012**, *22*(7), 1385–1390.

[49] Tonndorf, P.; Schmidt, R.; Bottger, P. Photoluminescence emission and Raman response of monolayer MoS_2, $MoSe_2$, and WSe_2. *Opt. Express* **2013**, *21*, 4908-4916.

[50] Cao, D.; Shen, T.; Liang, P. Role of chemical potential in flake shape and edge properties of monolayer MoS_2. *J. Phys. Chem.* **2015**, *119(8)*, 4294-4301.

[51] Yue, Q.; Chang, S.; Qin, S. Functionalization of monolayer MoS_2 by substitutional doping: a first principles study. *Phys. Lett.* **2013**, *377(19-29)*, 1362-1367.